

Detection prospects for the GW background of Galactic (sub)solar mass primordial black holes

Frans van Die,^a Ivan Rapoport,^a Yonadav Barry Ginat,^{b,c} and Vincent Desjacques^{a,d}

^aPhysics department, Technion, 3200003 Haifa, Israel

^bRudolf Peierls Centre for Theoretical Physics, University of Oxford, Parks Road, Oxford, OX1 3PU, United Kingdom

^cNew College, Holywell Street, Oxford, OX1 3BN, United Kingdom

^dAsher Space Research Institute, Technion, 3200003 Haifa, Israel

E-mail: frans.van@campus.technion.ac.il, ivanr@campus.technion.ac.il,
yb.ginat@physics.ox.ac.uk, dvince@physics.technion.ac.il

Abstract. In multi-component dark matter models, a fraction f_{pbh} of the dark matter could be in the form of primordial black holes (PBHs) with (sub)solar masses. Some would have formed binaries that presently trace the Milky Way halo of particle dark matter. We explore the gravitational wave (GW) signal produced by such a hypothetical population of Galactic PBH binaries and assess its detectability by the LISA experiment. For this purpose, we model the formation and evolution of early-type PBH binaries accounting for GW hardening and binary disruption in the Milky Way. Our analysis reveals that the present-day Galactic population of PBH binaries is characterized by very high orbital eccentricities $|1 - e| \ll 1$. For a PBH mass $M_{\text{pbh}} \sim 0.1 - 1 M_{\odot}$, this yields a GW background that peaks in the millihertz frequency range where the LISA instrumental noise is minimum. While this signal remains below the LISA detection threshold for viable $f_{\text{pbh}} \lesssim 0.01$, future GW observatories such as DECIGO and BBO could detect it if $0.01 \lesssim M_{\text{pbh}} \lesssim 0.1 M_{\odot}$. Furthermore, we anticipate that, after 5 years of observations, LISA should be able to detect $\mathcal{O}(100)$ (resp. $\mathcal{O}(1)$) loud Galactic PBH binaries of mass $M_{\text{pbh}} \sim 0.1 - 1 M_{\odot}$ with a SNR ≥ 5 if $f_{\text{pbh}} = 0.01$ (resp. $f_{\text{pbh}} = 0.001$). Nonlinear effects not considered here such as mass accretion and dynamical capture could alter these predictions.

Contents

1	Introduction	1
2	Formation of PBH binaries	3
2.1	Equation of motion	3
2.2	Time evolution of the reduced angular momentum	5
2.3	Properties of newly born PBH binaries	7
3	Evolution of Galactic PBH binaries	10
3.1	Early disruption by matter nonlinearities	10
3.2	Hardening through GW emission	11
3.3	Late-time disruption in the Milky Way halo	13
4	Galactic distributions	15
4.1	Galactic Double White Dwarfs	15
4.2	Galactic PBH binaries	17
4.3	Number of Galactic PBH binaries	18
5	Detecting Galactic PBH binaries	19
5.1	GW Energy Density	19
5.2	Confusion noise from unresolved Galactic DWDs	21
5.3	The GW background of Galactic PBH binaries	23
5.4	Loud Galactic PBH Binaries	26
6	Conclusions	30
A	Gravitational waves from eccentric compact binaries	31
A.1	Orbital evolution	31
A.2	Semi-numerical solution to the eccentric evolution	32
A.3	Spectral Distribution	34
B	Dynamical Friction in the Milky Way Halo	34

1 Introduction

Primordial black holes (PBHs) could have formed in the early Universe as a result of high-density fluctuations [1–5]. Interest in PBHs has surged since the LIGO-Virgo-KAGRA (LVK) experiments unveiled a population of black holes (BHs) with characteristic masses comparable or larger than the stellar-mass black hole candidates located in the Milky Way (MW) [6–8], which led to the suggestion that some of the black holes binaries detected by GW experiments are primordial [9, 10].

In contrast to earlier models where all dark matter (DM) was thought to consist of PBHs, it is now believed that PBHs could span a wide range of masses and represent only a fraction of the total energy density of a multi-component dark sector (for reviews, see [11, 12]

and references therein). The PBH abundance, as parameterized by the fraction of DM in the form of PBHs is written as

$$f_{\text{pbh}} = \frac{\Omega_{\text{pbh}}}{\Omega_{\text{DM}}} \quad (1.1)$$

Current observational constraints on PBH mass and abundance (summarized in [13, 14]) based on the microlensing of distant supernovae [15–18], cosmic microwave background (CMB) anisotropies [19, 20], gravimeter analyses [21, 22], observed GW events [e.g. 23] and interactions with compact stellar remnants [24, 25] yield an upper bound $f_{\text{pbh}} \lesssim 0.01$ for PBH in the mass window $10^{-2} - 10^3 \text{ M}_\odot$, with slightly tighter constraints at the high end of this mass window. Enhanced microlensing constraints with ROMAN could probe PBH fractions down to $f_{\text{pbh}} \sim 10^{-3} - 10^{-4}$ and may also investigate asteroid-mass PBHs [16, 26], which remain largely unconstrained [27]. While most constraints are derived from a monochromatic mass function, it's important to note that introducing extended mass functions can somewhat modify these constraints [e.g. 28].

Close pairs of PBHs can form binaries in the early Universe and emit GWs at frequencies dependent on their masses (for reviews, see [29–31]). They can merge by the present epoch if their initial eccentricity is close to unity [9, 32–35]. However, most of the PBH binaries that ever form will not have had enough time to have merged by now. These can be disrupted, or further harden through interactions with astrophysical objects or other PBHs. For low PBH fractions $f_{\text{pbh}} \lesssim 0.01$, consistent with current observational limits, PBH binaries get advected onto the dark matter halos [36–38] and masquerade as stellar BH binaries (some of which could reside in globular clusters, see [39]). In the MW halo, they would contribute to the Galactic GW background, which arises due to the superposition of many GW signals and can be probed by future GW space experiments such as the Laser Interferometer Space Antenna (LISA). Other Galactic sources of GWs include stellar compact binaries, to which $\sim 10^8$ double white dwarfs (DWDs) are the dominant contribution [40, 41].

The number N_0 of PBH binaries expected to reside in the MW halo is given by

$$N_0 = \frac{M_{\text{DM}}}{\text{M}_\odot} \frac{f_{\text{pbh}} \eta_0}{2m} \simeq 1.18 \times 10^{10} \text{ m}^{-1} \left(\frac{f}{0.01} \right) \eta_0 \quad (1.2)$$

assuming a MW dark matter mass of $M_{\text{DM}} = 2 \times 10^{12} \text{ M}_\odot$ [42, 43] and a monochromatic PBH mass spectrum with $M_{\text{pbh}} = m \text{ M}_\odot$. For convenience, we have introduced the fraction $f = 0.85 f_{\text{pbh}}$ of all matter in PBHs, while η_0 represents the fraction of Galactic PBHs that exist in a binary system at the present epoch. As we shall see later, $\eta_0 = \eta_0(f)$ is a function dependent mostly on f . For a PBH binary fraction of $\eta_0 \sim 0.1$ as advocated by [46] (which is fortuitously close to the fraction of white dwarfs in DWDs, see [40]) and for the parameter values $f \sim 0.01$ and $m \sim 1$, we find $N_0 \sim 10^9$ comparable to the number of DWDs in the MW. This motivates our calculation of the GW signal produced by a hypothetical population of Galactic PBH binaries. As we will see below, however, the spatial distribution and orbital parameters of Galactic PBH binaries differ significantly from those of the Galactic DWD population, even when the PBH mass falls in the solar mass range.

For the sake of generality, we remain agnostic about the precise formation mechanisms of PBHs and consider a multi-component DM scenario, in which a monochromatic population of PBHs of mass in the range $0.01 \leq m \leq 1000$ formed at the end of inflation and make up a fraction $f \leq 0.01$ of the total matter¹. We will be particularly interested in (sub)solar

¹See e.g. [44, 45] for studies involving a log-normal PBH mass distribution.

mass PBHs. Subsolar mass compact objects almost surely have a primordial origin [2], as standard stellar evolution models predict that stellar black holes should have masses exceeding solar [47], with the caveat that neutron stars and white dwarfs could theoretically be mildly subsolar in mass [48–50]. In the LVK O3 run, three subsolar mass compact object candidates were identified, though not confirmed due to their high false alarm rate [51, 52].

In this study, we concentrate solely on PBH binaries forming in the early Universe and discard the possibility that they interact with ordinary astrophysical objects to create mixed primordial-stellar binaries or triples [25, 53]. Therefore, the PBH binary population we are interested in is characterized by very high eccentricities. This distinguishes them from stellar BH binaries or PBH binaries forming in the late Universe via dynamical capture.

The paper is organized as follows. Sections §2 and §3 focus on the formation of PBH binaries from the RD era until the onset of nonlinear structure formation, and their survival in the MW halo until the present epoch. The present-day space distributions of Galactic PBH binaries and DWDs are modeled in Section §4. They provide the seed for the computation of the Galactic GW background and the extraction of loud Galactic PBH binaries discussed in Section §5. We conclude in §6.

2 Formation of PBH binaries

We initialize the PBH distribution at the end of inflation as a spatial Poisson process. We thus neglect spatial correlations in the initial clustering of PBHs, which depend heavily on the mechanism leading to PBH formation [e.g. 44, 45, 54–58]. We will also ignore the possibility that PBHs inherit a non-zero spin at formation [59].

For convenience, let $s = a/a_{\text{eq}}$ be the scale factor normalized to unity at matter-radiation (MR) equality. Throughout this section, we define s —comoving scales as equal to physical scales at MR equality, in contrast to regular comoving scales defined w.r.t. the present epoch. Let x_i represent the initial s —comoving distance (at the end of inflation) between nearest PBH neighbors, referred to as ‘PBH pairs’. The probability distribution $P(x_i)$ is given by

$$P(x_i) = 4\pi n x_i^2 \exp\left(-\frac{4\pi n x_i^3}{3}\right). \quad (2.1)$$

Here n is the s —comoving number density of PBHs,

$$n = \frac{f \rho_{\text{eq}}}{m M_{\odot}} \quad (2.2)$$

with

$$\rho_{\text{eq}} = \frac{\Omega_m}{a_{\text{eq}}^3} \frac{3H_0^2}{8\pi G} \simeq 1.7 \cdot 10^{-13} M_{\odot} \text{AU}^{-3} \quad (2.3)$$

given as the matter density at equality, and we have expressed the mass M_{pbh} of PBH as $M_{\text{pbh}} = m M_{\odot}$. For the range of f and m considered here, typical values of x are much lower than the s —comoving Hubble radius $\mathcal{H}_{\text{eq}}^{-1} \simeq 6 \cdot 10^9$ AU, so that we can compute the evolution of the distance to the nearest neighbor using a Newtonian approximation, as in [34].

2.1 Equation of motion

We model the time evolution of the proper separation r between nearest neighbor PBHs with

$$\ddot{r} - (\dot{H} + H^2)r + \frac{2GM}{r^2} \frac{r}{|r|} (1 - j^2) = 0, \quad (2.4)$$

where M is the total mass of the PBH pair, dots indicate differentiation with respect to cosmic time, $j \equiv j(t)$ represents the dimensionless or reduced angular momentum of the system,

$$j \equiv \frac{L}{m\sqrt{2Gmr}}. \quad (2.5)$$

and the Hubble rate (in a MR universe) is given by

$$H(s) = \left(\frac{8\pi G}{3} \rho_{\text{eq}} \right)^{1/2} h(s) \quad \text{with} \quad h(s) = \sqrt{s^{-3} + s^{-4}}, \quad (2.6)$$

A PBH pair forms a binary system at the time where $\dot{r} = 0$ for the first time, i.e. when the pair decouples from the Hubble flow. The newly-formed binary has properties that will, here and henceforth, be labeled with a $*$ subscript. In particular, the eccentricity of the binary at formation time follows from

$$j_* = \sqrt{1 - e_*^2} \quad (2.7)$$

A bound eccentric binary has $0 \leq e_* < 1$ by definition.

In this effective one-body approximation, it is essential to take into account the angular-momentum barrier, which leads to a large centrifugal force F_j for non-negligible j ,

$$F_j = \frac{L^2}{mr^3} = \frac{2GM^2j^2}{r^2}. \quad (2.8)$$

We immediately see in Eq. (2.4) that $j > 1$ prevents the PBH pair from ever decoupling from the Hubble flow as they will be on a hyperbolic orbit. As we will show shortly, the time dependence of j can prevent binary formation, even for initial values j_i significantly lower than unity, depending on the initial PBH density. For PBH binaries forming in the radiation-dominated (RD) era, eccentricities are very large ($|1 - e| \ll 1$) and the angular-momentum barrier can be safely neglected. It is, however, relevant for PBH binary formation in the matter-dominated (MD) era, where angular momentum grows with time. The next subsection is therefore dedicated to quantifying the physics of the angular-momentum barrier.

In order to evolve Eq. (2.3), it is convenient to introduce the time-independent variable

$$\lambda \equiv \frac{4\pi\rho_{\text{eq}}x_i^3}{3mM_{\odot}} \quad (2.9)$$

as well as the reduced separation $X \equiv r/(\lambda x_i)$ and the variable $\mathcal{S} \equiv s/\lambda$ as a proxy for time. This turns Eq. (2.4) into

$$X'' + \frac{2 + \lambda\mathcal{S}}{2 + 2\lambda\mathcal{S}} \frac{X - X'\mathcal{S}}{\mathcal{S}^2} + \frac{\mathcal{S}^2}{1 + \lambda\mathcal{S}} \frac{1}{\epsilon^2 + X^2} \frac{X}{|X|} (1 - j^2) = 0 \quad (2.10)$$

where a prime denotes differentiation with respect to \mathcal{S} and a small-scale cutoff ϵ is introduced to regularize the gravitational attraction of the PBHs in the limit $X \rightarrow 0$. A value of ϵ too small restricts the range of \mathcal{S} that can be probed numerically, whereas a value too large introduces errors in the determination of the reduced scale factor \mathcal{S}_* at which the PBHs decouple from the Hubble flow to form a binary. Eq. (2.10) shows that deep in the RD era, $\mathcal{S} \ll 1/\lambda$ and the gravitational pull is proportional to \mathcal{S}^2 while, in the MD era, it grows only as \mathcal{S} . Therefore binary formation is suppressed once the RD era ends. Ref. [34] were concerned mainly with PBH binaries merging at the present epoch, which form deep in the RD era. However, for the MW relics we are interested in, formation in the MD era is important, especially for low values of f (see Fig. 4).

2.2 Time evolution of the reduced angular momentum

The angular-momentum barrier depends on the external torques produced by distant PBHs and by fluctuations in the matter distribution [60, 61]. In what follows in later sections, we generally restrict ourselves to PBH scenarios with $f \lesssim 0.01$. Therefore, we can assume that the variations of j caused by distant PBHs and matter density fluctuations are mutually independent.

We initialize the initial angular momentum of the system by drawing its value $j_i = j_{pbh} + j_\delta$ from the sum of the independent variables j_{pbh} and j_δ encoding the angular momentum acquired through distant PBHs and matter fluctuations, respectively. This assumption leads to the probability density function (PDF) for j_i being constructed from the convolution

$$P(j_i) = P(j_{pbh}) * P(j_\delta). \quad (2.11)$$

Since the variables are independent, the mean and variance of j_i are additive:

$$\langle j_i \rangle = \langle j_{pbh} \rangle + \langle j_\delta \rangle \quad (2.12)$$

$$\text{Var}(j_i) = \text{Var}(j_{pbh}) + \text{Var}(j_\delta) \quad (2.13)$$

We adopt the distributions $P(j_{pbh})$ and $P(j_\delta)$ given in [34, 46]. Namely,

- For the torques produced by other PBHs, we use

$$P(j_{pbh}) = \frac{j_{pbh}}{j_f^2 [1 + (j_{pbh}/j_f)^2]^{3/2}} \quad (2.14)$$

where $j_f \equiv \frac{1}{2}\lambda f$ is a characteristic (and time-independent) angular momentum.

- For the torques generated by the matter perturbation δ_m dominated by the smooth or particle dark-matter (PDM) component, we take a Gaussian distribution:

$$P(j_\delta) = \frac{j_\delta}{\sigma_\delta^2} e^{-j_\delta^2/(2\sigma_\delta^2)} \quad (2.15)$$

This effect dominates for $f \ll 1$. The Gaussian distribution arises from the superposition of many large-scale linear perturbations. The mean and standard deviation are given by

$$\sigma_\delta^2 = \frac{3}{10} \sigma_{\text{eq}}^2 \lambda^2 = \text{Var}(j_\delta) \simeq \langle j_\delta \rangle^2 \quad (2.16)$$

where σ_{eq}^2 is the variance of linear matter density perturbations in the RD regime on comoving scales of the initial binary separation. Following [34], we take $\sigma_{\text{eq}} = 0.005$ for our numerical estimates². The numerical prefactor 3/10 arises from a directional averaging procedure involving the Gaussian tidal tensor (see Appendix 2 of [34]).

Torques induced by distant PBH and matter fluctuations are suppressed deep in RD, where the Hubble radius is not much greater than the separation of the PBH pair. These torques gradually increase toward MR equality such that, in the MD era, the reduced angular momentum of the system grows in proportion to the scale factor (see below), at least so long as

²In many scenarios PBH formation is accompanied by an enhancement of the primordial power at small scales [e.g. 62–66]. As a result, σ_{eq} might actually be higher. However, since the expected enhancement is strongly model-dependent, we shall ignore this effect.

linear cosmological perturbation theory is valid. For simplicity, we have assumed $j(t) = j_i$ constant throughout RD, with the distribution $P(j_i)$ spelled out above. A refined model for $j(t)$ in RD would not have changed our results significantly, since angular momentum accretion is small in the RD era, and PBH binaries forming before equality have high eccentricities $|1 - e_*| \lesssim 1$ [34, 46].

While we assume $j(t) = j_i$ throughout RD, we take into account the time-dependence of $j(t)$ in the MD era arising from the growth of matter perturbations, which dominates for $f \ll 1$. This time dependence is accounted for in the spirit of a mean-field approach, that is, it purely arises through the time dependence of $\langle j_\delta \rangle$ via Eq. (2.16). To ensure that this also holds in the MD era, we replace the constant σ_{eq} by a redshift-dependent rms variance σ_m such that $\langle j_\delta \rangle \propto \sigma_m$. Here, σ_m is the rms variance of matter fluctuations which in principle is to be computed as

$$\sigma_m^2(R, z) = \frac{1}{2\pi^2} \int_0^\infty dk k^2 P_m(k, z) W_R^2(k) \quad (2.17)$$

with $P_m(k, z)$ is the linear matter power spectrum at redshift z and $W_R(k)$ e.g. a top-hat filter. This expression depends on time through a growth rate squared present in $P_m(k, z)$, and through the (comoving) softening radius $R = (1+z)r(t)$ where $r(t)$ is the time-dependent physical scale of the PBH pair separation. For the m, f values considered here, R is very small relative to characteristic scales such as the Silk-damping scale, being at most of order a parsec deep in MD³. For simplicity, we ignore the time dependence of R and take $\sigma_m \simeq s\sigma_{\text{eq}}$. For PBH binaries forming late in the MD era, σ_m can therefore be 1 - 2 orders of magnitude larger than σ_{eq} until j starts to exceed unity.

Summarizing, the time dependence of the angular momentum in our mean-field approach is included in the following manner:

$$j(t) = j(s) = j_i + \sqrt{\frac{3}{10}} \lambda \sigma_{\text{eq}} \Xi(s) \quad (2.18)$$

where

$$\Xi(s) \equiv \begin{cases} 0 & s < 1 \\ s - 1 & s \geq 1 \end{cases} \quad (2.19)$$

This way, the constant torque from matter fluctuations in the RD era grows linearly with the scale factor after equality.

The initial, reduced angular momentum j_i is to be drawn randomly from a distribution $P(j_i)$, which is to be generated for various choices of (λ, f) . Transforming $P(j_i)$ to log-space $P(\log j_i)$ allows us to shift a template distribution to the desired range of j_i determined by parameters λ, f . In practice, we slightly loosen the interpretation of Eq. (2.13) such that both the expectation value and the typical angular momentum (the peak of the distribution) are expressed as the sum of the contributions arising from j_{pbh} and j_δ .

Fig. 1 shows $P(\log j_i)$ for various choices of λ . The two contributions to the torque have characteristic scales $j_f \sim \lambda f$ (for the other PBHs) and $j_\delta \sim \lambda \sigma_{\text{eq}}$ (for matter fluctuations). For $f \ll \sigma_{\text{eq}}$, the distribution $P(j_i)$ is therefore mostly determined by the matter fluctuations rather than by PBH torques. Only when $f \gtrsim \sigma_{\text{eq}}$ do the torque from other PBHs play a significant role.

³In principle one could also consider the free-streaming length of some WIMP DM particle λ_{fs} , and then take $R = (1+z)\max[\lambda_{fs}(m_X), r]$. We found this to be irrelevant for WIMPs in the mass range above MeV. Below this mass, speaking of WIMPs loses its meaning.

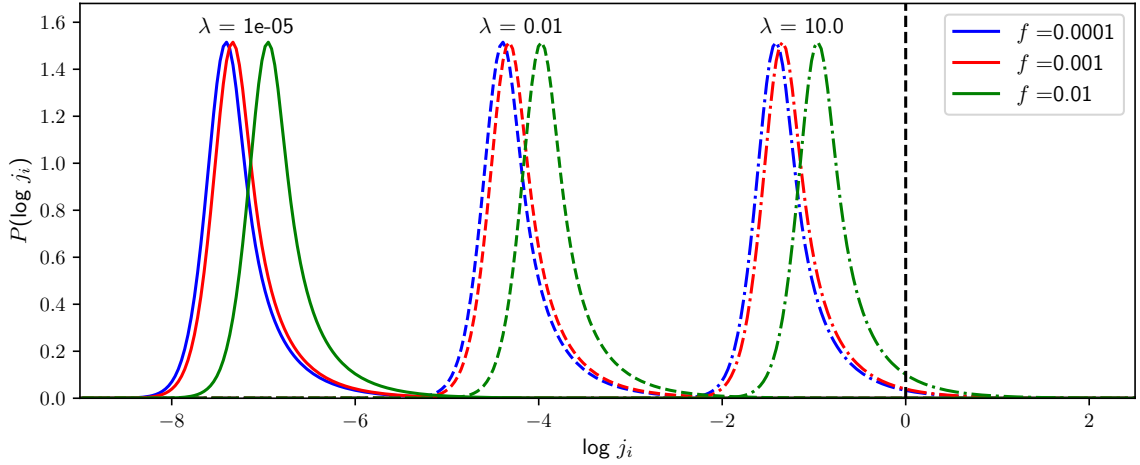


Figure 1: The distribution $P(\log j_i)$ of the reduced, initial angular momentum j_i of a PBH pair for different choices of λ . The solid curves assume the minimal value $\lambda = 10^{-5}$ of our parameter space, the dashed lines have $\lambda = 10^{-2}$ and the dashed-dotted distributions assume $\lambda = 10$, which is close to the maximum value of λ allowed for binary formation (see Fig. 3). The black dashed line shows $j_i = 1$, beyond which stable systems never form.

For PBH pairs with j_i exceeding unity, the angular-momentum barrier prevents decoupling from the Hubble flow and binary formation already in RD. Again we note that the growth of angular momentum according to Eq. (2.18) can also prevent binary formation in MD for lower initial $j_i < 1$, as we will be shown in the next Section.

2.3 Properties of newly born PBH binaries

We solve the equation of motion Eq. (2.10) for various values of λ . The initial conditions always match the Hubble flow, that is, $X(\mathcal{S} = 0) = 0$ and $X'(\mathcal{S} = 0) = 1$. We take $\epsilon = 10^{-20}$ in order to accurately determine the scale factor $s_*(\lambda) = \lambda \mathcal{S}_*(\lambda, j_i)$ at binary formation, which defines the formation redshift z_* and formation time t_* . The corresponding initial semi-major axis and angular momentum of the PBH binary are $a_*(\lambda) = \lambda x X_*(\lambda, j_i)/2$ and $j_* = j(s_*)$. Fig. 2 shows the outcome of the numerical evaluation of Eq. (2.10) for s_* and j_* as a function of λ and j_i .

The general trend seen in Fig. 2 can be explained by the facts that (i) larger values of λ imply larger initial separations x_i and later decoupling, while (ii) larger values of j_i increase the angular-momentum barrier and delay binary formation as well. From the left panel of Fig. 2, one might conclude that the parameter $\frac{\lambda}{1-j_i^2}$ primarily determines PBH binary formation. However, this observation only holds until MR equality ($\frac{\lambda}{1-j_i^2} \sim 1$), after which the time-dependence of the angular momentum dominates in delaying (and ultimately in preventing) the decoupling of PBH pairs from the Hubble flow. After MR equality, the initial parameter $\frac{\lambda}{1-j_i^2}$ alone is therefore insufficient to predict the properties of the newly-born PBH binary. Furthermore, note the absence of PBH binary formation beyond $s_{*,max} \sim 30$. At this point, the reduced angular momentum of the system exceeds unity, i.e. $j(t) > 1$ even for $j_i = 0$, such that binary formation in this manner becomes impossible after this point in time. The critical value of $s_{*,max} \sim 30$ can be inferred as follows: the left panel of Fig. 2 shows that s_*

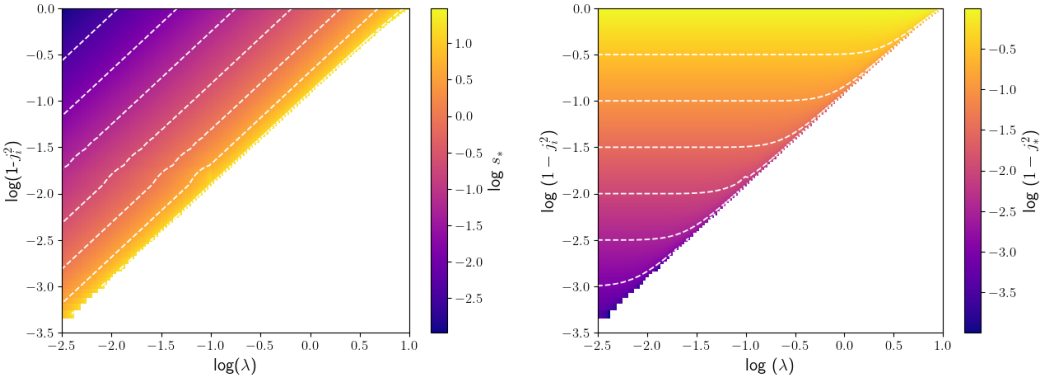


Figure 2: Contour levels of s_* (left panel) and $\log(1 - j_*^2)$ (right panel) in the $\log \lambda$ - $\log(1 - j_i^2)$ plane. A PBH pair with parameters in the white part of the parameter space does not decouple to form a binary. The left panel suggests the functional dependence $s_* = s_*(\frac{\lambda}{1 - j_i^2})$, which turns out to hold only up to MR equality $\frac{\lambda}{1 - j_i^2} \sim 1$. For $s_* > 1$, the angular-momentum barrier grows as seen in the right panel. This growth hinders the formation of PBH binaries after $s_* \sim 30$.

is maximum on a diagonal given by $\frac{\lambda}{1 - j_i^2} \sim 10$. On this diagonal, setting $j_i = 0$ yields $\lambda \sim 10$ which, once substituted into Eq. (2.18), leads to $j(t) \simeq 1$ when $s = s_{*,max} \sim 30$.

The approximate solutions $s_*(\lambda) \sim \lambda/3$ and $a_*(\lambda) \sim 0.1\lambda x$ found by [34] hold when binary formation occurs deep in the RD era, where the angular-momentum barrier is negligible. In this case, we have $\lambda, j_i \ll 1$ separately. These approximate solutions break down for binary formation around MR equality ($(\frac{\lambda}{1 - j_i^2}) \sim 1$) or further in the MD era. The reduced angular momentum j_* of the system at PBH binary formation follows from Eq. (2.18), i.e. $j_* = j_*(j_i, s_*(\lambda))$, while Eq. (2.7) determines the initial eccentricity e_* of the binary.

The properties of the newly-born PBH binaries are characterized by the distribution of the variables (a_*, s_*, j_*) , which are not independent. E.g. a_* is completely determined once j_* and s_* are known. In particular, the joint distributions $P(j_*, s_*)$ and $P(j_*, a_*)$ are fully specified by $P(j_i, \lambda)$, which is itself determined by $P(x_i)$ through

$$P(j_i, \lambda) = P(j_i|\lambda)P(\lambda) . \quad (2.20)$$

The conditional PDF $P(j_i|\lambda)$ is given by Eq. (2.11) and

$$P(\lambda) = P(x_i) \frac{dx_i}{d\lambda} = f e^{-f\lambda} . \quad (2.21)$$

Note that this expression is independent of the PBH mass m . Combining this with the angular momentum distribution $P(j_i)$ discussed above, we construct the PDF $P(\log j_i, \log \lambda)$, as shown in Fig. 3.

As seen in Fig. 3, a significant fraction of $P(\log j_i, \log \lambda)$ extends beyond the part of parameter space that results in decoupling. These represent PBH pairs that will not form a binary, since for a given j_i , increasing λ implies a stronger growth of the angular momentum barrier via Eq. (2.18). The angular-momentum barrier is thus even more likely to prevent the PBH pair from forming a bound system.

Transforming (j_i, λ) to the variables (s_*, a_*, j_*) , we compute $P(j_*, a_*)$, and the cumulative distribution $P(< s_*)$ upon marginalizing $P(j_*, s_*)$ over j_* . Note that, whereas both

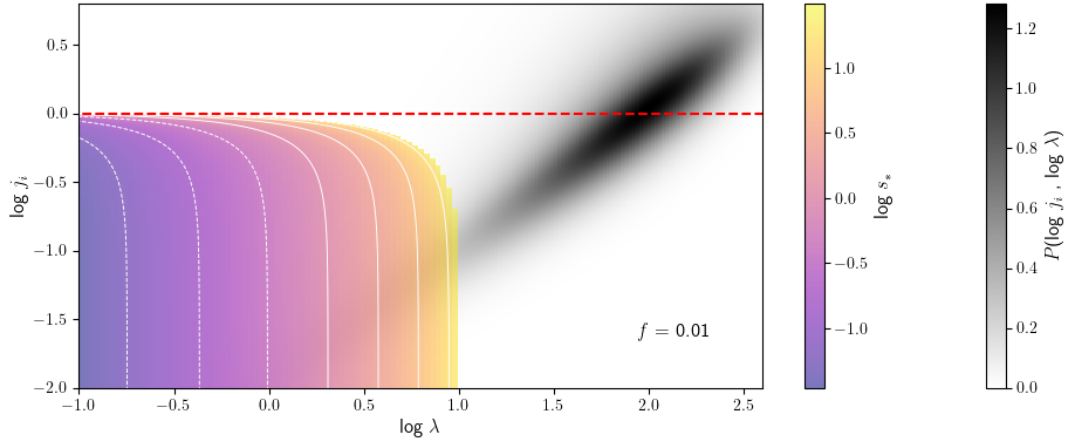


Figure 3: The gray-shaded area shows the joint distribution $P(\log j_i, \log \lambda)$ given by Eq. (2.20) for $f = 0.01$. The red dashed line indicates where j_i reaches unity. The angular-momentum barrier prevents PBH binary formation for large $\lambda \gtrsim 10$ even when $j_i <$ due to the time dependence of $j(t)$. Contour levels of the scale factor s_* are overlaid in color (as in Fig. 2).

$P(s_*, j_*)$ and $P(a_*, j_*)$ depend on f , only $P(a_*, j_*)$ depends also on the PBH mass m through the relation $a_*(\lambda) = \lambda x_i X_*(\lambda, j_i)/2$, with x_i related to the random variable λ according to Eq. (2.9).

The cumulative distribution $P(< s_*)$ is shown as the solid curves in Fig. 4, where only here and in Fig. 5 we include $f > 0.01$ for illustrative purposes. The deviation from the RD expectations (represented by the dashed curves) emphasizes the importance of taking into the angular-momentum barrier for binary formation in the MD era, especially for PBH models with $f < 1$. The transition to MD suppresses binary formation in two ways. First of all via the growth of the angular-momentum barrier of Eq. (2.18), and secondly due to the increase in the Universe's expansion rate in MD. Furthermore, we define η_* as the fraction of PBHs that eventually decouple to form a binary. η_* therefore equals the asymptotic value achieved by the cumulative PDF $P(< s_*)$. We observe that $\eta_* = \eta_*(f)$ is a decreasing function of f , with $\eta_* \sim 0.1$ for $f = 0.01$. We will return to this in Section §4.3.

Finally, Fig. 5 shows the joint distribution $P(j_*, a_*)$ for $m = 1$ and three choices of f . First, note that PBH binaries become wider as f is lowered, since the initial separation x_i increases when the PBH number density drops. Secondly, note that binary formation in MD is delayed due to the weakening of the effective gravitational attraction by the angular-momentum barrier (see Eq. (2.4)). For $f = 1$, Fig. 4 shows that only a small fraction of PBH pairs decouples in MD. Hence, only a small part of the PBH binary population shows the effect of a delay in decoupling, visible as a tail towards wide circular orbits in the top panel of Fig. 5. For lower values of f , most PBH binaries form in the MD era, which implies that the delay caused by the angular-momentum barrier affects nearly all of the PBH binary population, shifting it to higher a_* .

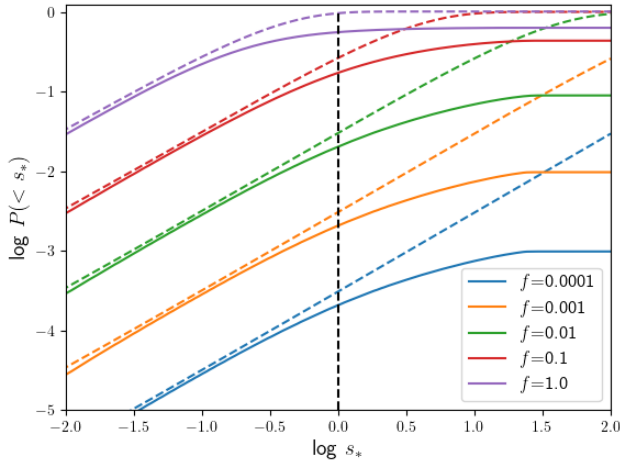


Figure 4: The cumulative distribution of the decoupling scale factor $P(< s_*)$. The dashed curves indicate the results assuming RD at all times and neglecting the angular-momentum barrier (a valid assumption in RD). The solid curves show the results for a universe with both matter and radiation, including the angular-momentum barrier. The vertical (black) dashed line marks MR equality. $P(< s_*)$ approaches a constant value $\eta_*(f) < 1$ in the limit $s_* \rightarrow \infty$, which reflects the suppression of PBH binary formation due to the angular-momentum barrier for $s_* > s_{*,max} \simeq 30$. The asymptotic value of $P(< s_*)$ represents the total binary-formation probability η_* .

3 Evolution of Galactic PBH binaries

Having discussed the formation of PBH binary systems in the early Universe, we need to evolve the systems to the present epoch, where the PBH binaries trace the MW DM halo. In this evolution process, we deal with three possible processes: early disruption by matter nonlinearities (which turns out to be satisfied automatically), GW hardening, and stellar disruption in the MW halo. These processes will be discussed separately below. Furthermore, since PBH models in the (sub)solar mass range with fractions $f > 0.01$ are severely constrained by microlensing events [17], we shall hereafter present results for $f \lesssim 0.01$ only.

3.1 Early disruption by matter nonlinearities

For PBH binaries decoupling from the Hubble flow in MD, nonlinear structures on the scale of the binary semi-major axis can significantly alter the simple scenario considered here. Nonlinear structures may disrupt the formation of PBH binaries. Moreover, nonlinearities in the matter distribution will quickly trigger star formation and, thereby, the formation of compact stellar remnants which could mimic PBHs when m is the solar mass range. To avoid these complications, we focus on "early-type" PBH binaries and discard those forming late in the MD era, when σ_m computed at redshift z_* and smoothed on scale a_* exceeds unity.

We find that "early-type" PBH binaries forming at redshift $z_* \lesssim 20$ should be discarded. As can be seen in Fig. 4, the angular-momentum barrier prevents binary formation already for $z_* \lesssim 100$. This implies that nonlinearities in the high-redshift matter density field do not alter the PBH binary distribution under consideration here.

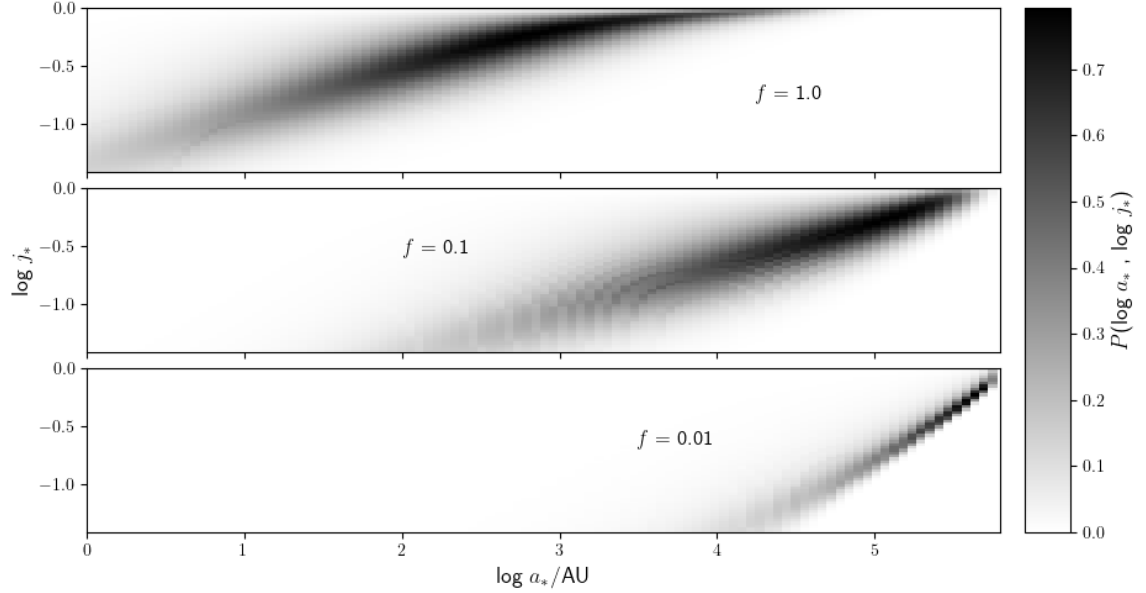


Figure 5: $P(\log a_*, \log j_*)$ for $m = 1$ and three choices for f . A different choice for m only slightly shifts the PDF towards higher semi-major axes. For $f < 0.01$, the distribution in a_*, j_* highly resembles the $f = 0.01$ (since the decoupling is mostly determined by the growing angular-momentum barrier early in the MD regime), with the difference mostly in $P(s_*)$ as can be seen from Fig. 4. All these PDFs have been normalized to 1 for visualization reasons.

3.2 Hardening through GW emission

As stated previously, knowledge of the parameters λ and j_* is all that is needed to determine the properties of newly born PBH binaries characterized by the values of (z_*, a_*, e_*) . Conservation of energy and angular momentum implies that the semi-major axis a and the eccentricity e of the PBH binary do not evolve independently. Assuming that PBH binaries only evolve through (vacuum) GW emission in the quadrupole approximation, the joint evolution of (a, e) follows from the coupled evolution equations for an eccentric orbit [67–69]

$$\begin{aligned} \frac{da}{dt} &= -\frac{128}{5} \frac{G^3 M^3}{c^5 a^3} \frac{1}{(1-e^2)^{7/2}} \left(1 + \frac{73}{24} e^2 + \frac{37}{96} e^4 \right), \\ \frac{de}{dt} &= -\frac{608}{15} \frac{G^3 M^3}{c^5 a^4} \frac{e}{(1-e^2)^{5/2}} \left(1 + \frac{121}{304} e^2 \right). \end{aligned} \quad (3.1)$$

where $M = 2mM_\odot$ is the total mass of the binary system. Note that Eqs. (3.1) are orbit-averaged evolution equations. In our situation of highly separated, very eccentric orbits, the orbital phase of the system may impact the exact radiative power significantly. However given that we deal with a large population of binaries, we assume that population-wise it is sufficient to work with these orbit-averaged evolution equations nonetheless. From these equations, the coalescence time t_{coal} of a binary with initial parameters a_*, e_* is given by

$$t_{\text{coal}} = \frac{5}{256} \frac{c^5 a_*^4}{G^3 M^2 \mu} F(e_*) \quad (3.2)$$

where $\mu = \frac{1}{2}mM_{\odot}$ is the reduced mass. The auxiliary function $F(e_*)$ is defined in Appendix §A, where it is also shown that the system (3.1) can be integrated to derive an analytical solution for the time needed to reach a new orbit with parameters (a, e) . This solution $t = t(a_*, e_*, e)$ is given by

$$t(a_*, e_*, e) = \frac{15}{304} \frac{c^5 a_*^4}{G^3 \mu M^2} \frac{I(e_*) - I(e)}{\mathcal{G}^4(e_*)} . \quad (3.3)$$

The function $I(e)$ can be expressed in terms of Appell hypergeometric functions (see Appendix A.2 for details). This expression can be (numerically) inverted to obtain the eccentricity $e(t, a_*, e_*)$ at time $t > t_*$ given the initial conditions (a_*, e_*) . The solution for $a = a(t, a_*, e_*)$ straightforwardly follows from Eq. (A.2)

The system (3.1) involves two distinct timescales t_a and t_e characterizing the evolution of a and e , respectively. t_a depends on a higher power of $(1 - e^2)$ and, therefore, is shorter than t_e . By neglecting $\mathcal{O}(1)$ contributions from the terms in the brackets in Eq. (3.1), the PBH binary evolves on a dynamical timescale t_a , which is initially

$$t_{a_*} \equiv \frac{c^5 a_*^4}{G^3 \mu M^2} (1 - e_*^2)^{7/2} . \quad (3.4)$$

Only PBH binaries with initial conditions (z_*, a_*, e_*) such that

$$t_{a_*} < \alpha t_H \quad (3.5)$$

will significantly evolve under GW emission within the age of the Universe t_0 . Here, t_H is the present-day Hubble time and $\alpha \geq 1$ generically. For PBH binaries that have not merged by the present epoch, we choose to evolve in time only those systems with $\alpha = 40$ in order to balance the computational cost (which becomes heavy when α is large) and the accuracy of the orbital evolution (which becomes poor when α is small). The PBH binaries with initial eccentricities and semi-major axes such that the binaries have already merged can be excluded from the present-day population.

Fig. 6 displays the final (present-day) semi-major axis and reduced angular momentum obtained from the computation of the orbital evolution under GW emission solely, for a model with $m = 1$ and $f = 0.01$. The PBH binaries that merge at the present epoch are located near the red spot, on the diagonal separating the red-shaded area from the colored one. The red spot approximately corresponds to the most probable values $a_* \sim 400AU$ and $j_* \sim 0.003$ for a merger at $t = t_0$. This agrees with the predictions of [34] (see their Fig. 4). For $\log \lambda \gtrsim 0.4$, evolution via GW emission is reduced because, in this part of the parameter space, the angular-momentum barrier increases so much that the characteristic GW evolution timescale becomes much larger than t_H .

The overlap between $P(j_i, \lambda)$ (shown as the grey-shaded area) and the region of the initial parameter space leading to a merger by $t \leq t_0$ (shown as the pink-shaded area) emphasizes that only a small fraction of PBH binaries that ever formed have merged by today. Likewise, only a small fraction of the PBH binaries (those close to the region of merger) significantly evolve via GW emission. For $m = 1$ and $f = 0.01$, only about 4% of the binaries have merged. This percentage does not change much for other choices of m and f , the highest merger fraction being $\sim 11\%$ for $m = 1000$ and $f = 0.0001$. Consequently, we will disregard hierarchical mergers and hierarchical binary formation in this study. This is also in line with our assumption of a constant f .

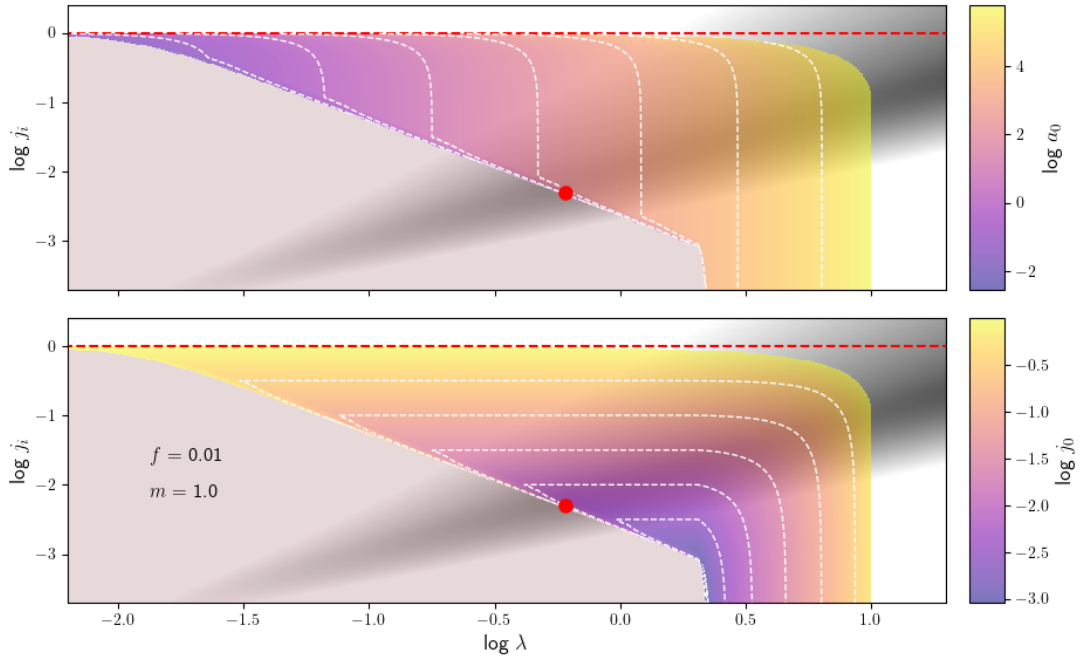


Figure 6: Semi-major axis and reduced angular momentum after evolution through GW emission for $m = 1, f = 0.01$. Dashed (white) curves indicate contours of constant a_0 (top panel) and j_0 (bottom panel) in the $\lambda - j_i$ plane. The pink-shaded area shows the initial parameter space leading to a merger by $t \leq t_0$. Mergers at $t = t_0$ have characteristic values of j_i and λ given approximately by the red dot. We have also overlaid the distribution $P(j_i, \lambda)$ as the grey-shaded area (as in Fig. 3) to emphasize that only a small fraction of PBH binaries merge by the present epoch.

At this point, we can evaluate the present-day PDF $\phi_{\text{pbh}}(a_0, j_0)$ of PBH binaries without the disruption effects that can take place in the MW halo (they will be discussed in Section §3.3). In Fig. 7, this PDF is shown for $f = 0.01$ and three choices of m . As stated earlier, the distribution doesn't change noticeably for different choices of $f < 0.01$, except for the number and fraction of PBH binaries. The key point here is that present-day PBH binaries are typically very eccentric and very wide and, therefore, will emit GWs at very high harmonics and mostly at pericenter passage. Additionally, it is important to note that despite the high eccentricity of the binaries, their pericenter distance remains sufficiently large to prevent substantial relativistic corrections in their orbital evolution.

3.3 Late-time disruption in the Milky Way halo

Once the MW halo has formed, the PBH binary can interact with MW stars and “field” PBHs (we ignore binary-binary interactions for simplicity), resulting in the disruption of the softest binaries. This effect depends on the stellar and PBH number density in the neighborhood of the PBH binary. As shown in Section §4, field PBHs and MW stars are distributed in up to four components (bulge, halo, thin disk, and thick disk). Consequently, the present-day space distribution $\phi_{\text{pbh}}(\mathbf{r})$ of PBH binaries and the distribution $\phi(a_0, e_0)$ of orbital parameters are not independent anymore once binary disruption is taken into account. Furthermore, binary

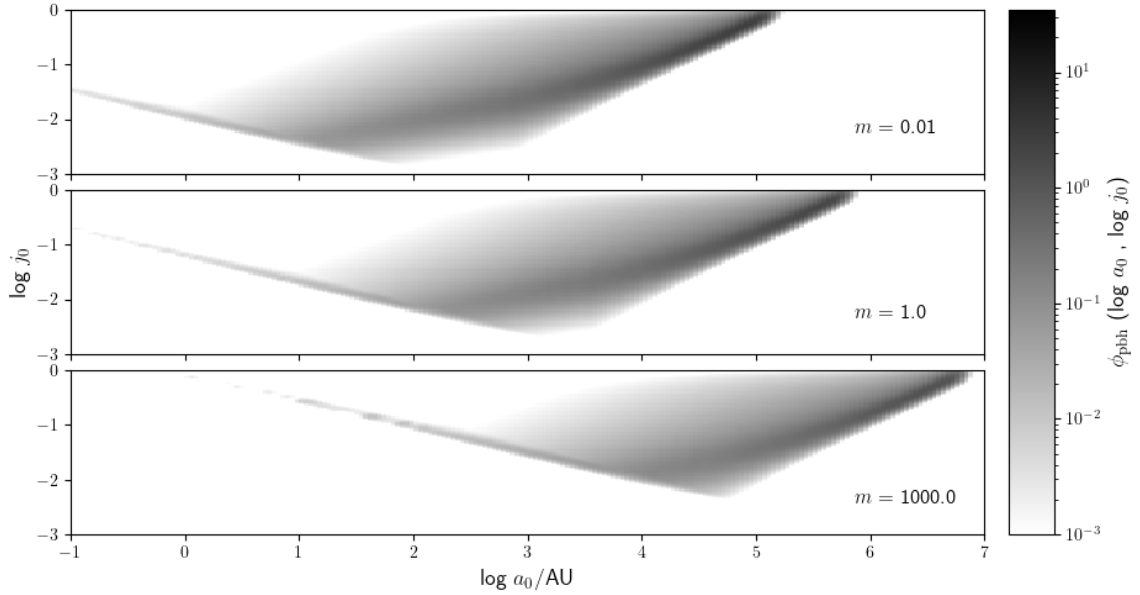


Figure 7: The present-day distribution $\phi_{\text{pbh}}(a_0, j_0)$ (shown with a logarithmic color scheme) for PBH binaries assuming $f = 0.01$ and three choices of m . The tail extending to smaller separations is caused by the loss of orbital energy through GW emission.

disruption is, in essence, probabilistic [see 70, 71]. For simplicity, however, we shall ignore its probabilistic nature and treat instead PBH binary disruption in a pure deterministic manner. Finally, we have ignored additional sources of disruption [reviewed in 72]⁴. In particular, we have neglected dynamical friction (DF) produced by the PDM component on the evolution of PBH binaries in the MW halo since, in the regime where DF is relevant, characteristic timescales for orbital-energy dissipation are much longer than disruption timescales (see Appendix §B). We have also ignored Galactic tides [75–77] because the time-scale of this process for $m \approx 1$ is too long for all but the widest binaries in the Galactic halo [76].

To encode PBH binary disruption, we introduce a function $\Pi_d = \Pi_d(\mathbf{r}, a_0)$, which equals 0 if a PBH binary with semi-major axis a_0 is disrupted at position \mathbf{r} , and 1 otherwise. Π_d depends also on the local stellar density $\rho_*(\mathbf{r})$ (calculated from the stellar MW profile described in Section §4) and PBH density $\rho_{\text{pbh}}(\mathbf{r})$ (calculated from the NFW profile Eq. (4.7)). We assume a total stellar mass in the MW of $5 \times 10^{10} \text{ M}_\odot$ [78–81], which (only for the disruption procedure) is taken to be fully made up by potentially-disrupting stars.

To define Π_d , we divide the present-day PBH binaries into two categories, based on their binding energy $E_b = Gm^2M_\odot^2/2a_0$ relative to the velocity dispersion of PBHs and MW stars, which we take to be $\sigma_v = 100 \text{ km/s}$ regardless of \mathbf{r} . For simplicity, we also assume encounters with MW stars of mass $m_* = 1\text{M}_\odot$ solely. Hard binaries, for which $E_b > m_*\sigma_v^2$,

⁴We also do not consider the case where one of the binary members might be replaced by a third object during a binary-single encounter [e.g. 71]. For hard binaries, the binary-single scattering cross-section in the stellar halo is small anyway, but also for soft binaries, we don't take general hardening evolution processes by 3-body encounters into account [73, 74]. Next to this, as is noted in [46], for $f \sim 1$, nearly all initial binaries are expected to be disrupted, based on simulations. Here $f \leq 0.01$, hence this is not the case here. Also [46] includes bound systems of several PBHs that can form around MR equality when $f \sim 1$. In the case $f \ll 1$, bound systems of more than 2 PBHs are highly unlikely to form.

Table 1: Parameters of the Galactic model spelled out in Eqs. (4.2-4.5), based on [85–88].

Length Scales (kpc)		Relative Weights	
h_{td}	0.3	f_{td}	0.84
h_{TD}	1	f_{TD}	0.05
H_{d}	3		
H_{b}	0.15	f_{b}	0.1
R_{h_*}	8	f_{h_*}	0.01

are not affected by any disruption effect [71]. However, soft binaries for which $E_b \leq m_* \sigma_v^2$ may be disrupted via two distinct channels (following Chapter 7 of [82]):

- Ionization, with a rate $R_I \simeq 27.03 \frac{G \rho_* a_0}{\sigma_v}$
- Evaporation, with a rate $R_E \simeq 16.39 \frac{\ln(\Lambda) G \rho_* a_0}{\sigma_v}$

Here, $\ln(\Lambda)$ is a Coulomb logarithm with $\Lambda \sim 0.6 \times \frac{m_* \sigma_v^2}{E_b}$. Hence, evaporation dominates for very soft binaries, while both processes contribute more or less equally when the binary is harder. A soft binary is assumed to be disrupted when $R_I + R_E > 1/t_H$. Note that this prescription is independent of the orbital phase and eccentricity ⁵.

For illustration, let us quantify how the disruption process affects the distribution shown in Fig. 7, which includes only binary hardening through GW emission. Fig. 8 shows the impact of disruption in three different MW environments or, equivalently, stellar densities: $\rho_* = 70 M_{\odot} \text{pc}^{-3}$ (for the MW bulge); $\rho_* = 0.06 M_{\odot} \text{pc}^{-3}$ (appropriate to the disk in the solar neighborhood); and $\rho_* = 2 \times 10^{-8} M_{\odot} \text{pc}^{-3}$ (for the stellar halo). In the latter case, we also take into account a contribution from field PBHs with density $\rho_{\text{pbh}} = 4 \times 10^{-7} M_{\odot} \text{pc}^{-3}$. In the halo, both the stellar and field PBH densities are too low to cause significant disruption effects⁶. The resulting distribution $\phi_{\text{disrupt}}(a_0, j_0)$ shown in Fig. 8 is identical to the distribution before including disruption except for a cut in semi-major axis. Results are shown for $f = 0.01$ and $m = 1$.

4 Galactic distributions

In this Section, we compute the spatial distribution of Galactic PBH binaries. Since the disruption of PBH binaries depends on the local stellar density, we begin with a model for the spatial distribution of MW stars. This profile serves a dual purpose, as it is also essential in the calculation of the GW foreground produced by Galactic DWDs.

4.1 Galactic Double White Dwarfs

The dominant component of the astrophysical compact binaries in the MW are $N_{\text{dwd}} \simeq 10^8$ double white dwarfs [e.g. 84]. DWDs provide a foreground to the GW signal produced by PBH binaries in the millihertz (mHz) frequency range probed by the LISA experiment. Hence accurate modeling of the DWD population is essential.

⁵A more realistic statistical implementation of the disruption process should take into account that the binary separation is smaller at pericenter and wider at apocenter.

⁶In [83], it has already been shown that fly-by events of single PBHs are expected only to have a subdominant effect on PBH binary properties.

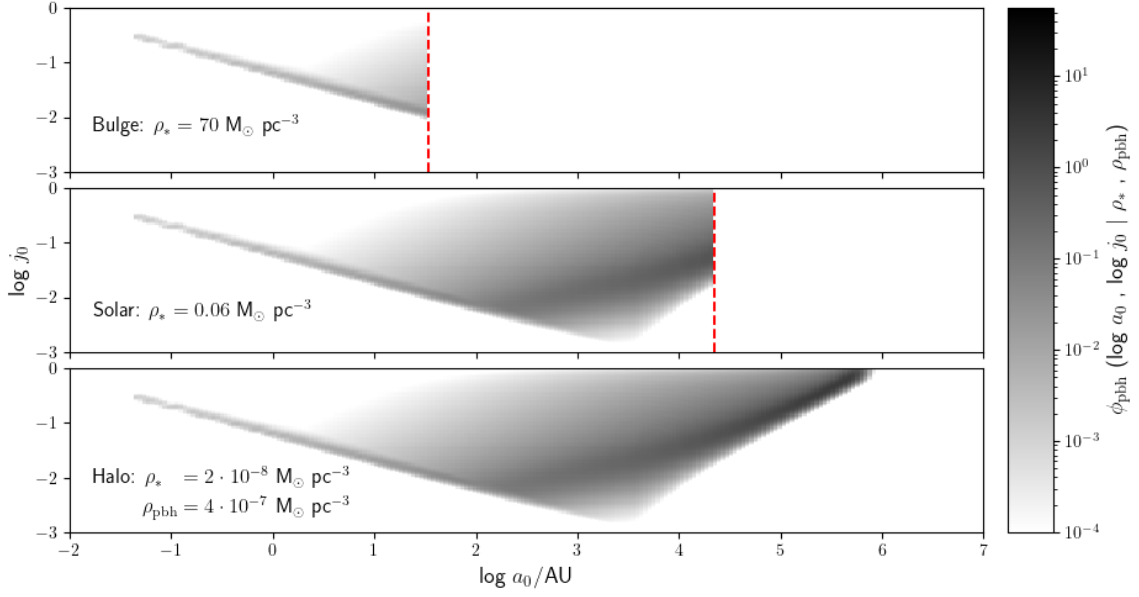


Figure 8: The effect of disruption on the parameter distribution $\phi(a_0, j_0)$ at three locations in the MW: the bulge, disk, and halo for a model with $m = 1, f = 0.01$. The region to the right of the red dashed line is disrupted at the respective locations. Note the logarithmic color scheme, showing that nearly all PBH binaries are disrupted in the bulge.

Assuming that the DWD population in the MW traces the stellar component, we follow [85–88] and express the probability $\phi_{\text{dwd}}(\mathbf{r}_g)$ for a DWD to be located at a separation \mathbf{r}_g away from the MW Galactic Center as

$$\phi_{\text{dwd}}(\mathbf{r}_g) = f_{\text{td}} \phi_{\text{td}}(\mathbf{r}_g) + f_{\text{TD}} \phi_{\text{TD}}(\mathbf{r}_g) + f_{\text{b}} \phi_{\text{b}}(\mathbf{r}_g) + f_{\text{h}_*} \phi_{\text{h}_*}(\mathbf{r}_g) , \quad (4.1)$$

where the probability densities $\phi_{\text{td}}(\mathbf{r}_g)$, $\phi_{\text{TD}}(\mathbf{r}_g)$, $\phi_{\text{b}}(\mathbf{r}_g)$ and $\phi_{\text{h}_*}(\mathbf{r}_g)$ are constructed from the Galactic profiles of the thin disk, thick disk, bulge and stellar halo, respectively. Furthermore, f_i are the relative weight of each component.

The disks decay exponentially in the Galactic plane $x - y$, while they quickly fall off along the vertical z -direction, where (x, y, z) are Cartesian coordinates relative to the Galactic Center:

$$\phi_{\text{td}}(\mathbf{r}_g) \propto \frac{e^{-\sqrt{x^2+y^2}/H_{\text{d}}}}{\cosh(z/h_{\text{td}})} \quad (4.2)$$

$$\phi_{\text{TD}}(\mathbf{r}_g) \propto \frac{e^{-\sqrt{x^2+y^2}/H_{\text{d}}}}{\cosh(z/h_{\text{TD}})} . \quad (4.3)$$

Their densities are expressed as a function of $x^2 + y^2$ because of cylindrical symmetry. The central bulge, on the contrary, is modeled as a simple radial exponential profile,

$$\phi_{\text{b}}(\mathbf{r}_g) \propto e^{-r_g/H_{\text{b}}} \quad (4.4)$$

where $r_g = |\mathbf{r}_g|$ is the radial distance from the Galactic Center. Finally, a small fraction of DWDs lives in the MW stellar halo, modeled as a Navarro-Frenk-White (NFW) profile [86]:

$$\phi_{\text{h}_*}(\mathbf{r}_g) \propto \frac{R_{\text{h}_*}}{r_g} \left(1 + \frac{r_g}{R_{\text{h}_*}}\right)^{-2} \quad (4.5)$$

The relative weights f_i of each component and the parameter values are summarized in Table 1. We assume there are no stars beyond a separation of 100 kpc from the Galactic Center.

The spatial distribution of Galactic DWDs is shown in the left panel of Fig. 9 in Galactic Coordinates (i.e. as viewed from the Sun). Note that the position of the Sun in the Cartesian coordinates used above is $\mathbf{r}_{g,\odot} = (8249, 0, 20.8)$ pc [89, 90], with the x -axis pointing towards the solar system.

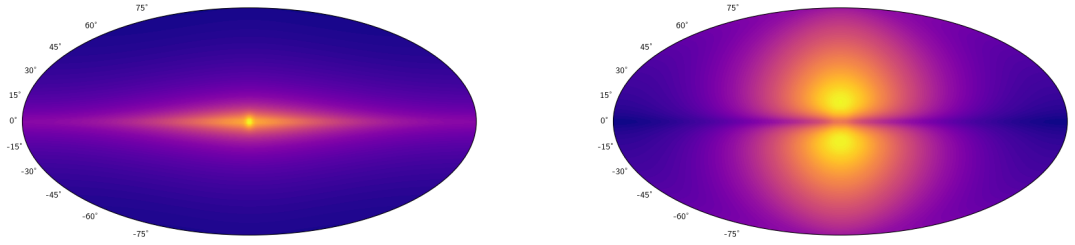


Figure 9: Angular maps of the sky density probability (i.e. integrated along the line of sight) of Galactic DWDs (left panel) and PBH binaries for $m = 1$, $f = 0.01$ (right panel). We observe that, due to stellar disruption, PBH binaries are mostly located in the halo, while DWDs are mostly concentrated in the disk and central bulge.

To model the GW power emitted by Galactic DWDs, we will also need their present-day semi-major axis and mass distributions. In this regard, we assume that the two white dwarf masses m_1 and m_2 follow a Gaussian distribution with mean $0.6M_\odot$ and standard deviation $0.1M_\odot$ [40]. Furthermore, we assume circular orbits with a semi-major axis a_{dwd} distributed according to the broken power law model of [84] ⁷:

$$\phi(a_{\text{dwd}}) \propto x^{4+\beta} \left[\left(1 + x^{-4} \right)^{\frac{\beta+1}{4}} - 1 \right] \quad (4.6)$$

with $x \equiv a_{\text{dwd}}/0.01\text{AU}$ and $\beta = -1.3$ and the distribution is ranging from a minimum separation of $14 \cdot 10^3$ km up to a maximum separation of 0.05 AU. As is also the case for the PBH binaries, the orbital inclination $\cos i$ of the DWDs is distributed uniformly.

4.2 Galactic PBH binaries

For the PBH fractions $f \lesssim 0.01$ considered here, the PDM component dominates the MW halo. We assume that the PDM distribution of the MW follows an NFW profile with a characteristic radius $R_{\text{h,dm}} = 20$ kpc, such that the total MW mass is $2 \times 10^{12} M_\odot$ and the local PBH+PDM density in the solar neighborhood is $\sim 0.01 M_\odot \text{pc}^{-3}$, i.e.

$$\phi_{\text{h,dm}}(\mathbf{r}_g) \propto \frac{R_{\text{h,dm}}}{r_g} \left(1 + \frac{r_g}{R_{\text{h,dm}}} \right)^{-2} \quad (4.7)$$

⁷If one would evolve the DWD population in time (as is the approach of [91, 92]), one could start from the initial binary separation distribution proposed by [40], which is the power law $\phi(a_{\text{dwd}}) \propto a^{-1.3}$.

where $r = |\mathbf{r}|$. Since PBHs are initially a Poisson sampling of the adiabatic mode, they behave as test particles advected by the PDM component. Therefore, we shall assume that the gravitational collapse and virialization of the MW halo lead to a distribution of PBHs that approximately traces the MW halo of particle DM (a small fraction of them could end up in globular clusters, see [39]). Hence we take the PBH spatial distribution to extend to the virial radius $R_{\text{vir}} \simeq 200$ kpc. However, the position-dependent disruption of PBH binaries by stars and field PBHs in the MW will cause their present-day distribution to deviate from the NFW profile. Therefore, the present-day spatial profile of PBH binaries in the MW is given by

$$\phi_{\text{pbh}}(\mathbf{r}_g) = \frac{1}{\eta_d} \int da_0 \phi_{\text{h,dm}}(\mathbf{r}_g) \phi(a_0) \Pi_d(a_0, \mathbf{r}_g) \quad (4.8)$$

where the distribution function $\Pi_d(a_0, \mathbf{r}_g)$ is defined in Section 3.3, the normalization factor η_d is defined below in Eq. (4.9) and $\phi(a_0)$ is computed by marginalizing $\phi(a_0, j_0)$ over j_0 , which can be done since disruption is taken to be independent of the eccentricity of the binary. The resulting spatial distribution of PBH binaries is shown in the right panel of Fig. 9 for an observer at the Sun. The symmetry of the PBH binary distribution around the vertical axis reflects the axial symmetry of the stellar components responsible for the disruption of PBH binaries in the Galactic disk.

4.3 Number of Galactic PBH binaries

The number N_0 of PBH binaries currently present in the MW halo depends on m and f according to Eq. (1.2). Three distinct physical effects determine the value of η_0 and thence on the characteristics of the present-day, Galactic PBH binary:

- Only a fraction $\eta_*(f)$ of all the PBHs form binaries (see §2). This is exemplified in Fig. 4. For low values of f , the large distance between nearest neighbors and the angular-momentum barrier counteracts binary formation.
- PBH binaries may merge due to the dissipation of orbital energy by GW emission (see §3.2). η_{merge} will denote the fraction of PBH binaries that have not merged by the present epoch.
- Galactic PBH binaries can be disrupted via stellar encounters (see §3.3). The fraction η_d of surviving binaries integrated over the MW halo can be expressed as

$$\eta_d = \int da_0 d\mathbf{r}_g \phi(a_0) \phi_{\text{h,dm}}(\mathbf{r}_g) \Pi_d(a_0, \mathbf{r}_g) . \quad (4.9)$$

Combining all these effects, the present-day fraction η_0 of MW PBHs in binary systems, relative to the total number of PBHs (see Eq. 1.2) reads

$$\eta_0 = \eta_* \cdot \eta_{\text{merge}} \cdot \eta_d \quad (4.10)$$

Since the dependence of η_0 on m and f is known, the degeneracy in Eq. (1.2) between η_0 and f is now broken. The fractions η_{merge} and η_d are larger than ~ 0.9 and ~ 0.98 respectively for the values of m and f under consideration. This implies that η_0 is primarily determined by $\eta_* = \eta_*(f)$, which is a function of f solely. The left panel of Fig. 10 exemplifies the weak dependence of η_0 on m . The right panel of Fig. 10 demonstrates that there are still regions

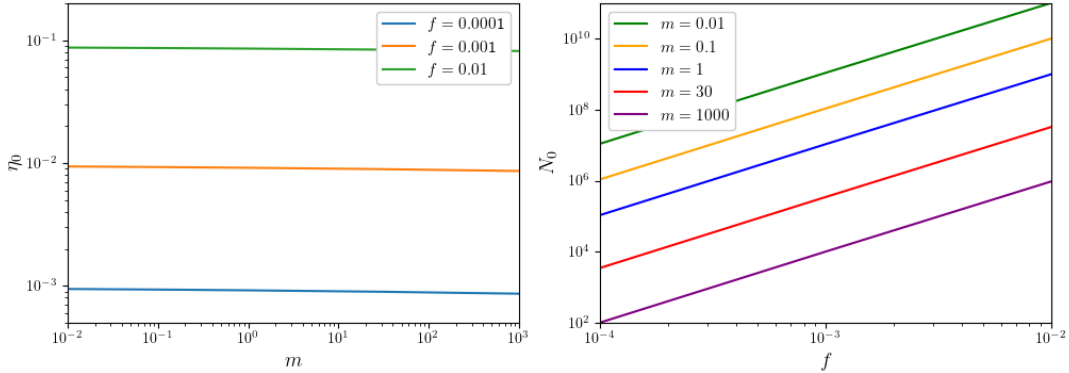


Figure 10: *Left panel:* Fraction η_0 of PBHs in the MW that live in a binary system. η_0 is mainly determined by $\eta_* = \eta_*(f)$, with a weak m -dependence arising through η_{merge} and η_{d} . *Right panel:* total number N_0 of Galactic PBH binaries for different choices of m and f .

of the m - f parameter space for which N_0 is comparable to or larger than the number $N_{\text{dwd}} \sim 10^8$ of Galactic DWDs.

To conclude, note that we have assumed throughout that both m and f remain constant in time. In particular, we have neglected the growth of PBH mass via merger and accretion and the possibility that second-generation PBH binaries may form. These evolution effects will effectively lower f in time. However, since we have found that $1 - \eta_{\text{merge}}$ (which can be thought of as a proxy for the PBH merger rate) to be quite low, these effects will likely result in small corrections to the simplified scenario considered here.

5 Detecting Galactic PBH binaries

In this Section, we explore the feasibility of detecting a GW background arising from the hypothetical population of Galactic PBH binaries, focusing on the LISA experiment. The detectability of this background depends on the level of the confusion noise of unresolved Galactic DWDs. We will not consider e.g. the GW signal produced by extragalactic DWDs [93].

5.1 GW Energy Density

We compute the GW energy density (per logarithmic frequency interval $d \ln \nu$)

$$\Omega_{\text{gw}}(\nu) \equiv \frac{1}{\rho_c} \frac{d\rho_{\text{gw}}}{d \ln \nu} \quad (5.1)$$

sourced by Galactic DWDs and PBH binaries based on their present-day parameter distributions (unlike, e.g. [92], who expressed Ω_{gw} in terms of the source parameter distribution at formation time). Here, ν is the observed frequency of the gravitational waves. We gather the source parameters in the vector ξ . Accounting for the sky-dependence of the signal and the orbital inclination ι of the binary sources, $\Omega_{\text{gw}}(\nu)$ is fully specified by the probability distribution $\phi(\mathbf{r}, \xi, \iota)$, where \mathbf{r} is the separation vector between the Earth and the source. For a uniformly distributed inclination angle, we can write

$$\phi(\mathbf{r}, \xi, \iota) d\mathbf{r} d\xi d\cos \iota = \frac{1}{2} \phi(\mathbf{r}, \xi) d\mathbf{r} d\xi d\cos \iota. \quad (5.2)$$

With these definitions, $\Omega_{\text{gw}}(\nu)$ can be expressed as [e.g. 92, 94]

$$\Omega_{\text{gw}}(\nu) = \frac{8\pi^2 N \nu^3}{3H_0^2 F} \left\langle \left| \tilde{h}_{\nu,i} \right|^2 \right\rangle_{r,\xi,i} = \frac{8\pi^2 N \nu^3}{3H_0^2 F} \int d\mathbf{r} d\xi \phi(\mathbf{r}, \xi) \left\langle \left| \tilde{h}_{\nu,i} \right|^2 \right\rangle_i. \quad (5.3)$$

Here, N is the total number of sources, and $\tilde{h}_{\nu,i} \equiv \tilde{h}_\nu(\mathbf{r}, \xi, i)$ is the discrete Fourier transform of the GW signal produced by a single source in the MW. We keep the dependence on i explicit in the shorthand notation for reasons that will become clear below. The notation $\langle \dots \rangle_X$ indicates an ensemble average over the parameter X . Furthermore, the division by the angular form factor $F \equiv \langle F^+ \rangle_{\hat{\mathbf{n}}} + \langle F^\times \rangle_{\hat{\mathbf{n}}}$ of the GW detector cancels out a similar factor in $\langle |\tilde{h}_{\nu,i}|^2 \rangle_i$ and ensures that $\Omega_{\text{gw}}(\nu)$ is independent of the detector configuration.

For the LISA experiment, we have

$$\mathcal{R} \equiv \langle F^+ \rangle_{\hat{\mathbf{n}}} = \langle F^\times \rangle_{\hat{\mathbf{n}}} \simeq \frac{3}{10}, \quad (5.4)$$

where \mathcal{R} is the signal response function averaged over the sky and the polarization of the GWs. At higher order, \mathcal{R} is frequency dependent. We shall stick to the first order approximation, valid up to frequencies $\lesssim 10^{-2}$ Hz above which the sensitivity of the LISA interferometer is significantly reduced [95]. Therefore, Eq. (5.4) implies $F = 2\mathcal{R} = 3/5$ for LISA (note that $F = 2/5$ for the LIGO experiment).

When the source emits at a single frequency as is the case for circular binaries, the discrete Fourier transforms $\tilde{h}_{\nu,i}$ are related to the Fourier modes $\tilde{h}(\nu_2, i) \equiv \tilde{h}(\nu_2, r, \xi, i)$ of the whole continuous signal of a single source through [e.g. 92]

$$\tilde{h}_{\nu,i} = \tilde{h}(\nu_2, i) \frac{\Pi_T(\nu)}{\sqrt{T}} \quad (5.5)$$

where ν is the observed frequency, ν_2 is the (quadrupole) GW frequency of the source, equaling $\nu_2 \equiv 2\nu_0(\xi)$ with ν_0 the orbital frequency. Furthermore, $\Pi_T(\nu)$ is the window function of an experiment with duration time T . On taking $T \rightarrow 0$, we have

$$\lim_{T \rightarrow 0} \frac{\Pi_T(\nu)}{T} = \left| \frac{d\nu}{dt} \right| \delta(\nu - \nu_2). \quad (5.6)$$

This is the relevant limit in our case too, where the sources do not evolve significantly throughout the observational run. The Fourier modes are then given by

$$\tilde{h}(\nu_2, i) = h_0(\nu_2, r, \xi) e^{i\Psi(\xi)} \mathcal{F}(i), \quad (5.7)$$

where $h_0(\nu_2, r, \xi)$ is the amplitude of the inspiral waveform (to be specified shortly) and $e^{i\Psi(\xi)}$ is its phase. The latter cancels out in the expression of $\Omega_{\text{gw}}(\nu)$. Moreover, the complex form factor $\mathcal{F}(i)$ depends on the orbital inclination. It can be approximated by [95] ⁸:

$$\mathcal{F}(i) = \sqrt{\mathcal{R}} \left(\frac{1 + \cos^2 i}{2} + i \cos i \right) \quad (5.8)$$

⁸In this way $\tilde{h}(\nu_2, i)$ is independent of the angular position on the sky. Especially in the case of anisotropic sources, the total strain is correlated with the angular sky location, depending on the detector orientation. A more precise method would be to use the complicated separate polarization form factors F^+, F^\times , as outlined in e.g. [96]. In this work, we neglect this technicality for simplicity. This is also justified by the added uncertainty around LISA's orientation and finalized design.

Averaging over the inclination angle $0 \leq \iota < \pi$ gives

$$\langle \mathcal{F}(\iota) \mathcal{F}^*(\iota) \rangle_\iota = \frac{4}{5} \mathcal{R} = \frac{2}{5} F. \quad (5.9)$$

Combining all the above expressions, we arrive at

$$\Omega_{\text{gw}}(\nu) = \frac{16\pi^2 N \nu^3}{15 H_0^2} \int d\mathbf{r} d\boldsymbol{\xi} \phi(\mathbf{r}, \boldsymbol{\xi}) \left| \frac{d\nu}{dt} \right| \delta(\nu - \nu_2) h_0^2(\nu_2, r, \boldsymbol{\xi}) \quad (5.10)$$

The dependence on the sky direction arises only through $\phi(\mathbf{r}, \boldsymbol{\xi})$, which encodes the spatial density of sources in the MW. One should bear in mind that Eq. (5.10) is strictly speaking only valid for circular orbits. We will generalize this expression to eccentric orbits in Section §5.3 when we discuss PBH binaries.

5.2 Confusion noise from unresolved Galactic DWDs

The confusion noise from unresolved Galactic DWDs is computed by assuming circular orbits, with the waveform given by

$$h_0(\nu_2, r, \boldsymbol{\xi}) = \frac{1}{\pi^{2/3}} \sqrt{\frac{5}{24}} \frac{c}{r} \left(\frac{GM_c}{c^3} \right)^{5/6} \nu_2^{-7/6} \quad (5.11)$$

where $M_c = (m_1 m_2)^{3/5} (m_1 + m_2)^{-1/5}$ is the chirp mass of the binary system. The parameter vector $\boldsymbol{\xi}_{\text{dwd}}$ of the DWD is composed of the semi-major axis a_{dwd} , the masses \mathfrak{m}_1 and \mathfrak{m}_2 of the individual white dwarfs, and the spatial location \mathbf{r} of the system in Galactic Coordinates. The distributions for these parameters are given in Section 4.1.

We use a_{dwd} to eliminate the Dirac delta in Eq. (5.10). As a result, the GW energy density $\Omega_{\text{dwd}}(\nu)$ of the Galactic DWD foreground reads

$$\begin{aligned} \Omega_{\text{dwd}}(\nu) &= \frac{16\pi^2 N_{\text{dwd}} \nu^3}{15 H_0^2} \int d\mathbf{r} d\boldsymbol{\xi}_{\text{dwd}} \phi_{\text{dwd}}(\mathbf{r}, \boldsymbol{\xi}_{\text{dwd}}) \left| \frac{d\nu}{dt} \right| \delta(\nu - \nu_2) h_0^2(\nu_2, r, \boldsymbol{\xi}_{\text{dwd}}) \\ &= \frac{16\pi^2 N_{\text{dwd}} \nu^3}{15 H_0^2} \int d\mathbf{r} d\mathfrak{m}_1 d\mathfrak{m}_2 \phi_{\text{dwd}}(\mathbf{r}, \boldsymbol{\xi}_{\text{dwd}}) \left| \frac{da_{\text{dwd}}}{dt} \right| h_0^2(\nu, r, \boldsymbol{\xi}_{\text{dwd}}) \Big|_{a_{\text{dwd}}=a_{\text{dwd}}(\nu, \mathfrak{m}_1, \mathfrak{m}_2)}, \end{aligned} \quad (5.12)$$

where $\nu_2 \equiv \nu_2(\boldsymbol{\xi}_{\text{dwd}})$, a_{dwd} is fixed by the other parameters. Kepler's law and the relation $\nu = 2\nu_o$ between ν and the orbital frequency ν_o appropriate for circular orbits give

$$a_{\text{dwd}}(\nu, \mathfrak{m}_1, \mathfrak{m}_2) = \left(\frac{G(\mathfrak{m}_1 + \mathfrak{m}_2)}{\pi^2} \right)^{1/3} \nu^{-2/3}. \quad (5.13)$$

Combining this expression with orbital decay timescale via GW emission yields

$$\left| \frac{da_{\text{dwd}}}{dt} \right| = \frac{64\pi^2}{5} \frac{G^2 \mathfrak{m}_1 \mathfrak{m}_2}{c^5} \nu^2. \quad (5.14)$$

Some of the Galactic DWDs will significantly exceed the LISA noise level. Their signal will be subtracted from the total GW strain to produce a confusion noise of unresolved DWDs with a GW energy density $\Omega_{\text{ndwd}}(\nu) \leq \Omega_{\text{dwd}}(\nu)$.

To implement the extraction of loud DWDs, and thereby maximizing the SNR of the PBH binary GW signal, let us first specify the LISA sensitivity, which is encoded in the effective noise power spectral density $S_n(\nu)$ given by

$$S_n(\nu) \equiv \frac{P_n(\nu)}{\mathcal{R}}. \quad (5.15)$$

Here, $P_n(\nu)$ the power spectral density of the detector noise. On substituting $\mathcal{R} = 3/10$, we obtain the following analytic fit for the noise [95]:

$$S_n(\nu) \simeq \frac{10}{3} \left(P_{\text{OMS}}(\nu) + \frac{2P_{\text{acc}}(\nu)}{(2\pi\nu)^4} \left[1 + \cos^2 \left(\frac{\nu}{\nu_*} \right) \right] \right) \times \left[1 + 0.6 \left(\frac{\nu}{\nu_*} \right)^2 \right] \quad (5.16)$$

where, for sake of completeness, $\nu_* = 19.09$ mHz is a characteristic frequency, while the optical metrology and test mass acceleration noises are respectively given by [97]

$$\begin{aligned} P_{\text{OMS}}(\nu) &= 3.6 \cdot 10^{-41} \text{ Hz}^{-1} \times \left(1 + \left[\frac{2 \text{ mHz}}{\nu} \right]^4 \right) \\ P_{\text{acc}}(\nu) &= 1.44 \cdot 10^{-48} \text{ Hz}^{-1} \times \left(1 + \left(\frac{0.4 \text{ mHz}}{\nu} \right)^2 \right) \times \left(1 + \left[\frac{\nu}{8 \text{ mHz}} \right]^4 \right). \end{aligned} \quad (5.17)$$

This model assumes a LISA arm length $L = 2.5 \times 10^9$ m.

A source is deemed loud when the inclination and polarization-averaged signal-to-noise ratio (SNR) χ exceeds a critical signal-to-noise ratio χ_c , where for the DWDs, we take a fixed value $\chi_c = 8$. The SNR is computed as follows [92, 95]:

$$\chi^2 = 4 \int d\nu \frac{\bar{h}^2(\nu)}{S_n(\nu)} \Pi_T(\nu) \quad (5.18)$$

where we have defined

$$\bar{h}^2(\nu) \equiv \frac{\langle \tilde{h}(\nu, \iota) \tilde{h}^*(\nu, \iota) \rangle_\iota}{\mathcal{R}} = \frac{4}{5} h_0^2(\nu, r, \xi). \quad (5.19)$$

Note that the parameter vector ξ does not include the inclination ι , which is averaged out from this expression. On using Eq. (5.6), we obtain

$$\begin{aligned} \chi^2 &= \frac{16}{5} T \int d\nu \left| \frac{d\nu}{dt} \right| \delta(\nu - \nu(r, \xi)) \frac{h_0^2(\nu, r, \xi)}{S_n(\nu)} \\ &= \frac{16}{5} T \left(\left| \frac{d\nu}{dt} \right| \frac{h_0^2(\nu, r, \xi)}{S_n(\nu)} \right)_{\nu=\nu(r, \xi)}. \end{aligned} \quad (5.20)$$

The LISA observation-time window T is set to $T = 5$ years from here on.

The subtraction of loud DWDs above the LISA noise can be conveniently captured by the function Θ_n defined as

$$\Theta_n(r, \xi_{\text{dwd}}) \equiv H(\chi_c - \chi(r, \xi_{\text{dwd}})),$$

where $H(x)$ is the Heaviside step function ($H(x) = 1$ for $x \geq 0$, and zero otherwise). The energy density of the confusion noise of unresolved DWDs follows from the insertion of Θ_n into the expression Eq. (5.10) of the unsubtracted GW energy density, i.e.

$$\Omega_{ndwd}(\nu) = \frac{16\pi^2 N_{dwd} \nu^3}{15 H_0^2} \int d\mathbf{r} d\mathbf{m}_1 d\mathbf{m}_2 \phi_{dwd}(\mathbf{r}, \boldsymbol{\xi}_{dwd}) \left| \frac{da_{dwd}}{dt} \right| \times h_0^2(\nu, r, \boldsymbol{\xi}_{dwd}) \Theta_n(\mathbf{r}, \boldsymbol{\xi}_{dwd}) \Big|_{a_{dwd}=a_{dwd}(\nu, \mathbf{m}_1, \mathbf{m}_2)}. \quad (5.21)$$

The effect of the subtraction of loud DWD sources on the energy density of the Galactic GW background is shown in Fig. 11. For convenience, we have defined a dimensionless noise spectral power

$$\Omega(\nu) = \frac{4\pi^2}{3H_0^2} \nu^3 S(\nu) \quad (5.22)$$

analogous to the energy density of the actual GW signals. Furthermore, we have assumed an observational time window of $T = 5$ yr. The confusion noise of unresolved DWD GW sources represented by the dashed blue curve is consistent with other estimates from the literature [84, 98–104]. The solid red curve is the effective noise level which we shall adopt for our assessment of the detectability of Galactic PBH binaries.

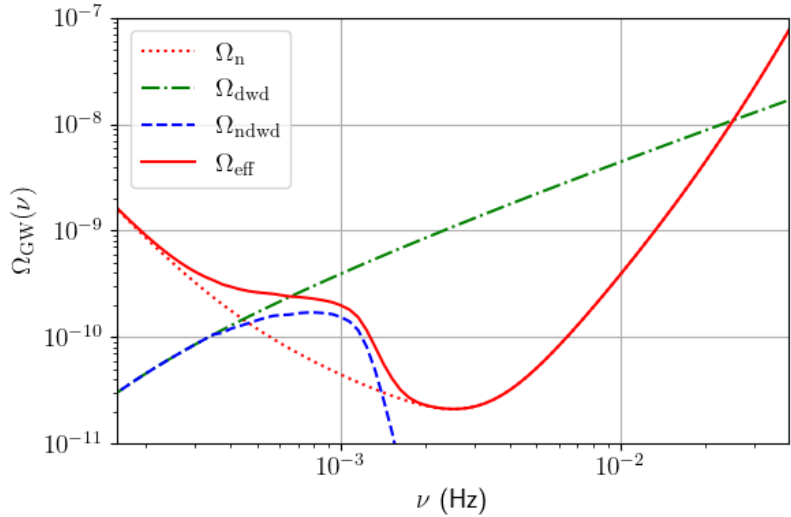


Figure 11: The dotted-dashed (green) curve is the GW energy density $\Omega_{dwd}(\nu)$ of the unsubtracted foreground of Galactic DWDs. The dashed (blue) curve represents the energy density of the confusion noise $\Omega_{ndwd}(\nu)$ left over after the subtraction of loud DWD sources (blue dashed) in a $T = 5$ yr LISA observational run with $\chi_c = 8$. The dotted (red) curve shows the LISA instrumental noise, while the solid (red) curve is the effective LISA noise $\Omega_{\text{eff}} = \Omega_{ndwd} + \Omega_n$ we use for the search of Galactic PBH binaries.

5.3 The GW background of Galactic PBH binaries

In contrast to DWDs, Galactic PBH binaries are highly eccentric and thus emit GW radiation across a large number of harmonic frequencies $\nu_n \equiv n\nu_0$ (where $n \geq 1$ is any positive integer)

of the fundamental (orbital) frequency ν_0 . We refer the reader to Appendix §A.3 for a brief review of the spectral distribution of eccentric GW sources.

Computing the exact, time-domain waveform of a GW signal produced by an eccentric compact binary remains a difficult task (see, e.g., [105, 106] for recent attempts). Therefore, we take another route and introduce an effective, orbit-average strain $h_{0,n}$ following the methodology of [102, 107–110]. To define $h_{0,n}$, let us recast the GW energy spectrum into the form given in [94],

$$\Omega_{\text{gw}}(\nu) = \frac{1}{\rho_c} \int d\mathbf{r} d\boldsymbol{\xi} n(\mathbf{r}, \boldsymbol{\xi}) \frac{1}{4\pi r^2} \frac{dE_{\text{gw}}}{d\ln \nu} . \quad (5.23)$$

Here, $\rho_c = 3c^2 H_0^2 / 8\pi G$ is the present-day critical density, $n(\mathbf{r}, \boldsymbol{\xi})$ is the number density of sources per unit distance along the line of sight with location \mathbf{r} and parameter $\boldsymbol{\xi}$. In addition, $dE_{\text{gw}}/d\nu$ is the energy radiated by a single source in the frequency interval $[\nu, \nu + d\nu]$. The factor of $(4\pi r^2)^{-1}$ arises because E_{gw} is a luminosity (integrated over solid angles) rather than a flux. It is given by

$$\frac{dE_{\text{gw}}}{d\ln \nu} = \frac{dE}{dt} \nu \frac{dt}{d\nu} = P \frac{\nu}{\dot{\nu}} = P \left| \frac{T}{\dot{T}} \right| , \quad (5.24)$$

where P is the power radiated in GWs and T is the orbital period. First, consider circular sources for which only the $n = 2$ harmonics contribute. We have

$$\frac{dE_{\text{gw}}}{d\ln \nu} = \frac{dE_{e=0}}{d\ln \nu_2} = P_{e=0} \left| \frac{T}{\dot{T}} \right|_{e=0} = \frac{\pi^{2/3}}{3} \frac{(GM_c)^{5/3}}{G} \nu_2^{2/3} . \quad (5.25)$$

Here, $E_{e=0}$ and $P_{e=0}$ are the GW energy and power radiated by a circular source at the quadrupolar frequency $\nu_2(\boldsymbol{\xi})$, respectively. Substituting this result into Eq. (5.23), we arrive at

$$\Omega_{\text{gw}}(\nu) = \frac{16\pi^2 \nu^3}{15H_0^2} \int d\mathbf{r} d\boldsymbol{\xi} c n(\mathbf{r}, \boldsymbol{\xi}) h_0^2(\nu_2, r, \boldsymbol{\xi}) . \quad (5.26)$$

Comparing this expression with Eq. (5.10), we can identify an event rate per line of sight distance, and per unit spatial and parameter volume according to

$$c n(\mathbf{r}, \boldsymbol{\xi}) = N \phi(\mathbf{r}, \boldsymbol{\xi}) \left| \frac{d\nu}{dt} \right| \delta(\nu - \nu_2) \quad (5.27)$$

Consider now eccentric binaries which radiate GWs in all the harmonics $\nu_n(\boldsymbol{\xi}) = n\nu_0(\boldsymbol{\xi})$. Denoting the GW energy and power radiated in the n th harmonic by $E_n(e)$ and $P_n(e)$, respectively, $dE_n(e)/d\ln \nu$ is

$$\frac{dE_n(e)}{d\ln \nu_n} = P_n(e) \left| \frac{T}{\dot{T}} \right|_{e \neq 0} = \frac{\pi^{2/3}}{3} \frac{(GM_c)^{5/3}}{G} \nu_n^{2/3} \times \left(\frac{2}{n} \right)^{2/3} \frac{g(n, e)}{f(e)} . \quad (5.28)$$

The factor of $1/f(e)$ arises through $|T/\dot{T}|_{e \neq 0}$ whereas $g(n, e)$ emerges from the power P_n radiated in the n th harmonics. The quantities $P_{e=0}$, $P_n(e)$, $g(n, e)$ and $f(e)$ are all defined in Appendix §A.3. Eqs. (5.26) and (5.27) show that the generalization of $\Omega_{\text{gw}}(\nu)$ to eccentric sources is

$$\Omega_{\text{gw}}(\nu) = \frac{16\pi^2 N \nu^3}{15H_0^2} \sum_{n=1}^{\infty} \int d\mathbf{r} d\boldsymbol{\xi} \phi(\mathbf{r}, \boldsymbol{\xi}) \left| \frac{d\nu}{dt} \right| \delta(\nu - \nu_n) h_{0,n}^2(\nu_n, r, \boldsymbol{\xi}) . \quad (5.29)$$

We have introduced an effective orbit-average strain

$$h_{0,n}(\nu_n, \mathbf{r}, \boldsymbol{\xi}) \equiv h_0(\nu_n, \mathbf{r}, \boldsymbol{\xi}) \sqrt{\gamma_n(e)} \quad (5.30)$$

$$\gamma_n(e) \equiv \left(\frac{2}{n}\right)^{2/3} \frac{g(n, e)}{f(e)},$$

which captures the orbit-averaged GW emission by eccentric sources. For large eccentricities $1-e \ll 1$ the function $g(n, e)$ peaks at harmonic number $n_{\max} \sim (1-e^2)^{-3/2} \sim j^{-3}$ [111]. For a Galactic PBH binary with a typical reduced angular momentum value of $j \sim 10^{-2} - 10^{-1}$, the peak of GW emission occurs at harmonic numbers $n_{\max} \sim 10^3 - 10^6$, that is, at a frequency orders of magnitude larger than ν_0 .

Specializing Eq. (5.29) to the Galactic population of PBH binaries, we have

$$\Omega_{\text{pbh}}(\nu) = \frac{16\pi^2 N_0 \nu^3}{15 H_0^2} \sum_{n=0}^{\infty} \int d\mathbf{r} d\boldsymbol{\xi}_{\text{pbh}} \phi_{\text{pbh}}(\mathbf{r}, \boldsymbol{\xi}_{\text{pbh}}) \left| \frac{d\nu}{dt} \right| \delta(\nu - \nu_n(\boldsymbol{\xi}_{\text{pbh}})) h_0^2(\nu, \mathbf{r}, \boldsymbol{\xi}_{\text{pbh}}) \gamma_n(e_0) \quad (5.31)$$

The vector of binary parameters $\boldsymbol{\xi}_{\text{pbh}}$ comprises the reduced angular momentum j_0 and the semi-major axis a_0 of the binary. There is no integral over a PBH mass due to the assumption of a monochromatic mass function. Taking into account Galactic disruption, the distribution function ϕ_{pbh} is given as:

$$\phi_{\text{pbh}}(\mathbf{r}, \boldsymbol{\xi}_{\text{pbh}}) = \phi_{\text{h,dm}}(\mathbf{r}) \phi_{\text{pbh}}(a_0, j_0) \Pi_{\text{d}}(a_0, \mathbf{r}) \quad (5.32)$$

To simplify the calculation of Eq. (5.31), we take advantage of the large expected n_{peak} and approximate the sum of harmonic numbers by a continuous integral, ignoring the remainder term of the Euler-MacLaurin formula. Furthermore, in complete analogy with the calculation of Ω_{gw} for Galactic DWDs, we get rid of the Dirac delta by integrating over the semi-major axis a_0 to obtain

$$\Omega_{\text{pbh}}(\nu) = \frac{16\pi^2 N_0 \nu^3}{15 H_0^2} \int d\mathbf{r} dj_0 dn \phi_{\text{pbh}}(\mathbf{r}, \boldsymbol{\xi}_{\text{pbh}}) \left| \frac{da_0}{dt} \right| h_0^2(\nu, \mathbf{r}, \boldsymbol{\xi}_{\text{pbh}}) \gamma_n(e_0) \Big|_{a_0=a_0(\nu, n, \boldsymbol{\xi}_{\text{pbh}})} \quad (5.33)$$

Note that a_0 is now a function of ν and n because the orbital frequency satisfies $\nu_0 = \nu_n/n \equiv \nu/n$. In the particular case of equal-mass binaries with non-zero eccentricity, we have

$$a_0(\nu, n, m) = \left(\frac{n^2 G m \text{ M}_\odot}{2\pi^2} \right)^{1/3} \nu^{-2/3}. \quad (5.34)$$

In addition,

$$\left| \frac{da_0}{dt} \right| = \frac{64\pi^2}{5} \frac{G^2 (m \text{ M}_\odot)^2}{c^5} \left(\frac{2}{n} \right)^2 \nu^2 f(e_0), \quad (5.35)$$

which cancels the multiplicative factor of $1/f(e_0)$ present in $\gamma_n(e_0)$.

The results of this computation are shown in Fig.12, where the various colored curves show $\Omega_{\text{pbh}}(\nu)$ for different choices of m and f as quoted on the figure. We have applied a Gaussian kernel of rms width 0.06 dex in log space to reduce the numerical noise. The (black) solid curve indicates the effective LISA noise level including the DWD confusion noise, as

calculated in Section §5.2. For $m = 0.1$ and 1 , which bracket the DWD mass range, the peak frequency of $\Omega_{\text{pbh}}(\nu)$ lies around the minimum of the effective noise even though the bulk of Galactic PBH binaries have semi-major axes much larger than 1 AU. The reason is the presence of extremely high harmonics induced by highly eccentric motions, which shift the peak of the GW emission frequency to much higher frequencies relative to wide but circular binaries. We also observe that lower mass PBHs exhibit a peak at larger frequencies due to their lower typical separation (see Fig. 7). Furthermore, increasing f by one order of magnitude increases Ω_{GW} by approximately two orders of magnitude, such that $\Omega_{\text{pbh}}(\nu)$ for a model with $f = 0.1$ and $m = 1$ (not shown on this figure) would be above the effective LISA noise. For reference, we also indicate in Fig. 12 the expected sensitivity curve of the Decihertz Interferometer Gravitational-Wave Observatory (DECIGO) [112] and the Big Bang Observer (BBO) [113] in their most simple design as reported by [114]. These experiments should be able to detect the background produced by Galactic subsolar mass PBHs down to mass $m = 0.01$ if $f \simeq 0.01$.

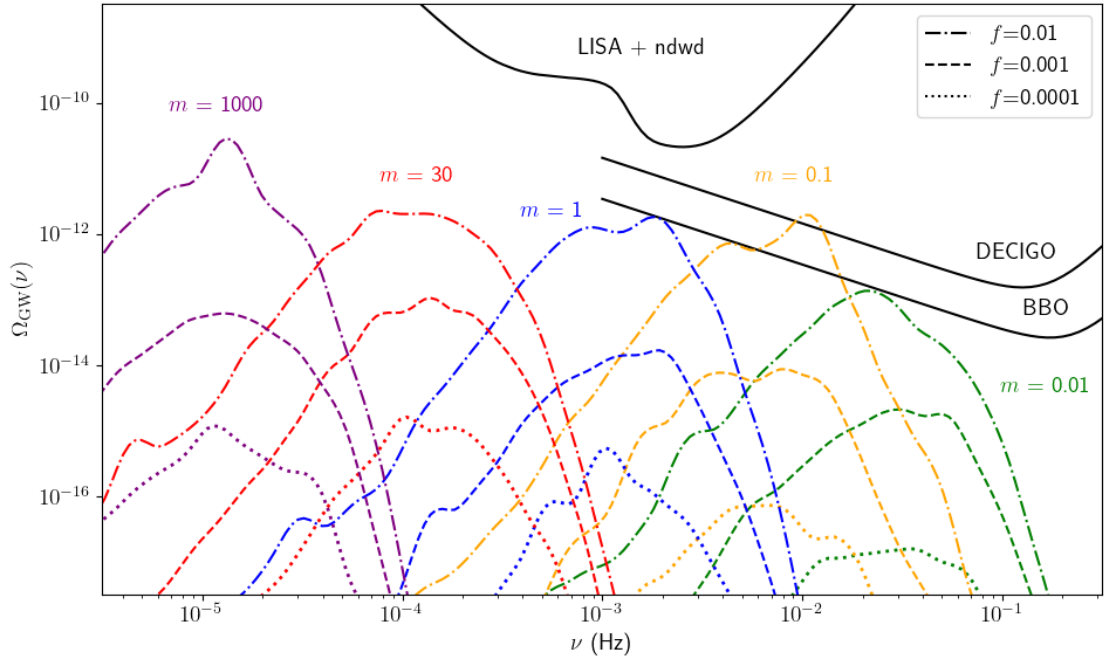


Figure 12: The GW energy density $\Omega_{\text{pbh}}(\nu)$ of a Galactic population of PBH binaries as a function of the observed GW frequency ν . Results are shown for different choices of m and f . The solid black curve represents the effective LISA noise level, which includes the confusion noise of unresolved Galactic DWDs. The sensitivity curves of the DECIGO and BBO experiments are taken from [114].

5.4 Loud Galactic PBH Binaries

The identification of loud PBH binaries in the Milky Way is analogous to the extraction of loud Galactic DWDs performed above, expect that we adopt a total noise power spectral density $S_{\text{eff}} = S_{\text{n}} + S_{\text{ndwd}}$. Accounting for the non-zero eccentricity of the Galactic PBH

binaries, the SNR χ_{pbh} is given by

$$\begin{aligned}\chi_{\text{pbh}}^2 &= \frac{16}{5} T \sum_{n=0}^{\infty} \left(\left| \frac{d\nu}{dt} \right| \frac{h_{0,n}^2(\nu, \mathbf{r}, \boldsymbol{\xi})}{S_{\text{eff}}(\nu)} \right)_{\nu=\nu_n(\mathbf{r}, \boldsymbol{\xi})} \\ &\simeq \frac{16}{5} T \int d\nu \left(\left| \frac{d\nu}{dt} \right| \frac{h_{0,n}^2(\nu, \mathbf{r}, \boldsymbol{\xi})}{S_{\text{eff}}(\nu)} \right)_{\nu=\nu_n(\mathbf{r}, \boldsymbol{\xi})}\end{aligned}\quad (5.36)$$

where T is, again, the LISA observational time window which we set to $T = 5$ yr hereafter. Note that $h_{0,n}$ is an orbit-average strain and so is χ_{pbh} . However, one should bear in mind that, for highly eccentric orbits, most of the GW power is emitted around pericenter passage in a burst of GWs [see 115, 116, for a recent discussion]. For the whole population of Galactic PBH binaries, this burst emission averages out but, for the small expected number of loud sources, it may play a role depending on their eccentricities. We will come back to this point once the loud sources have been identified.

A PBH binary is deemed loud if it satisfies $\chi_{\text{pbh}}(\mathbf{r}, \boldsymbol{\xi}_{\text{pbh}}) > \chi_c$, where, just as for the DWD foreground, χ_c is the detection threshold. A reasonable detection threshold is $\chi_c \sim 7 - 8$, whereas $\chi_c = 1$ corresponds to a typical fluctuation. In Fig. 13, regions of the a_0 - j_0 parameter subspace for which the condition $\chi_{\text{pbh}}(\mathbf{r}, \boldsymbol{\xi}_{\text{pbh}}) = \chi_c$, is fulfilled with $\chi_c = 1$ or $\chi_c = 8$ are shown as the dashed and solid curves, respectively. Loud sources mostly emerge from the tail of the distribution produced by Galactic PBH binaries having significantly hardened through GW emission. Therefore, they are hardly affected by disruption processes taking place in the MW. For illustration, we have assumed that the loud sources reside in the MW halo (where binary disruption is certainly negligible, see §3.3) and are located at a distance $r = 100$ pc and 10 kpc from the Sun. Note that, while the present-day distribution of PBH binaries in the MW halo (shown as the shaded area) depends on the PBH fraction, contours of constant SNR are independent of f .

The expected number N_{loud} of loud Galactic PBH binaries detected by LISA after 5 years of observation is

$$N_{\text{loud}} = N_0 \int d\mathbf{r} d\boldsymbol{\xi}_{\text{pbh}} \phi_{\text{pbh}}(\mathbf{r}, \boldsymbol{\xi}_{\text{pbh}}) \tilde{\Theta}_{\text{t}}(\mathbf{r}, \boldsymbol{\xi}_{\text{pbh}}) \quad (5.37)$$

where the “clipping” function $\tilde{\Theta}_{\text{t}}$ is

$$\tilde{\Theta}_{\text{t}}(\mathbf{r}, \boldsymbol{\xi}_{\text{pbh}}) \equiv H(\chi_{\text{pbh}}(\mathbf{r}, \boldsymbol{\xi}_{\text{pbh}}) - \chi_c) . \quad (5.38)$$

In practice, we not not take into account disruption in the computation of N_{loud} since, as stated above, it is irrelevant for the loud sources. Furthermore, in the computation of the SNR, we use the sky-averaged effective noise level S_{eff} given by the sum of the sky-averaged DWD noise and the sky-averaged LISA instrumental noise. This approximation is conservative for PBH binaries in the MW halo, where the foreground of unresolved DWDs is reduced relative to the disk or its sky-averaged value ⁹.

The expected number of loud sources are shown in the left panel of Fig. 14 for different choices of χ_c . A conservative detection threshold of $\chi_c = 8$ leads to ~ 20 loud sources in 5 years LISA data for $m = 0.1, 1$ and $f = 0.01$. For the other parameter choices, χ_c must be

⁹Incorporating the precise angular dependence of the LISA instrumental noise levels is beyond the scope of this paper.

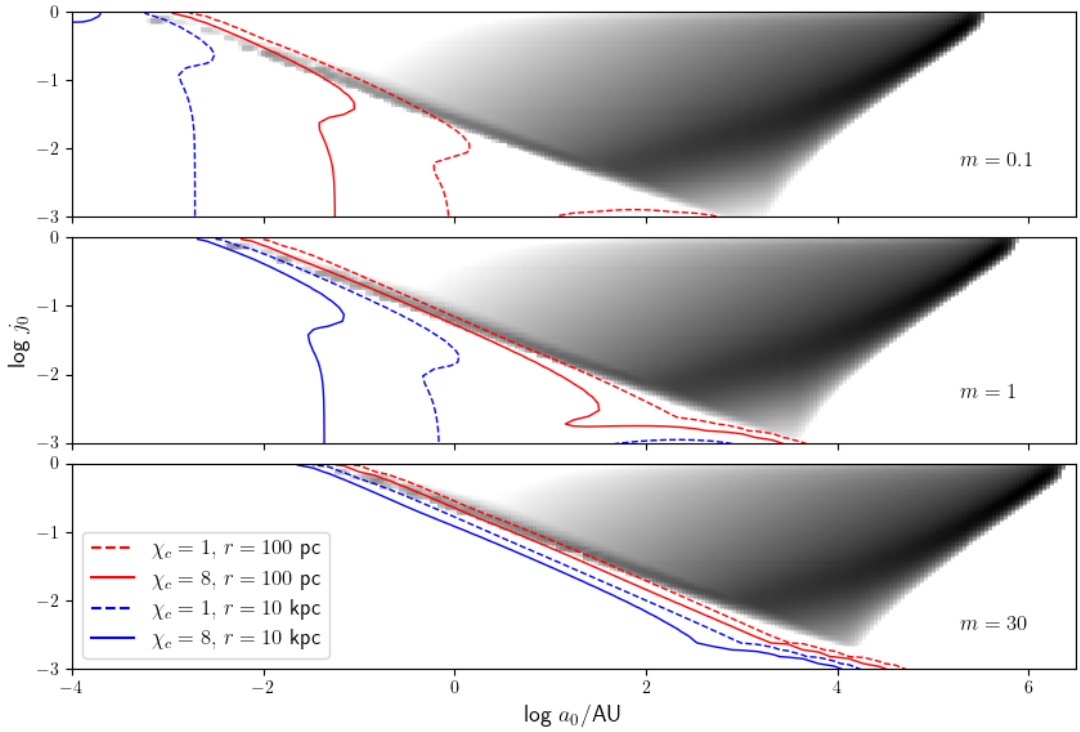


Figure 13: The dashed and solid curves indicate the locus in the a_0 - j_0 plane for which $\chi_{\text{pbh}}(\mathbf{r}, \xi_{\text{pbh}}) = \chi_c$. The loud sources with SNR exceeding χ_c are located leftward of the various curves, which assume Galactic PBH binaries residing in the MW halo at a distance $r = 100$ pc and 10 kpc from the Sun. The dark shaded area represents the present-day distribution of MW halo PBH binaries for a PBH fraction $f = 0.01$. Note, however, that contours of constant SNR are independent of f . Results are shown for 3 different values of m (panels from top to bottom)

decreased for the cumulative count $N_{\text{loud}}(> \chi_c)$ of loud PBH binaries to exceed unity (For $m = 1000$ not shown here, N_{loud} is far below unity even for $\chi_c = 1$). Overall, the latter increases with decreasing χ_c following a power law $N_{\text{loud}}(> \chi_c) \propto \chi_c^{-\gamma}$. The power law index would be $\gamma = 3$ for a homogeneously distributed population since the detection rate then scales linearly with spatial volume. This power-law is also consistent with a strain probability density function $P(h) \sim h^{-4}$ at large h [91], which gives $dN/d\chi_c \propto \chi_c^{-4}$ [92]. Deviations from $\gamma = 3$ are caused by the inhomogeneity of the spatial distribution of Galactic PBH binaries (which traces the MW halo). More precisely, cumulative counts with power law indices further away from $\gamma = 3$ correspond to distance distributions dN_{loud}/dr reaching larger separations (where the effects of the inhomogeneous spatial PBH profile are larger). This is quite apparent in the middle panel of Fig. 14, where the loud PBH binaries in the $m = 1$ model are distributed further away than in the $m = 0.1$ model. The increase in the characteristic distance of loud sources thus leads to a decrease in spatial homogeneity and results in a larger deviation from $\gamma = 3$. This correlation holds also for the models not shown in Fig. 14. The right panel of Fig. 14 shows that, unlike the bulk of the Galactic PBH binaries, the loud sources are only mildly eccentric, with typical eccentricities ~ 0.7 .

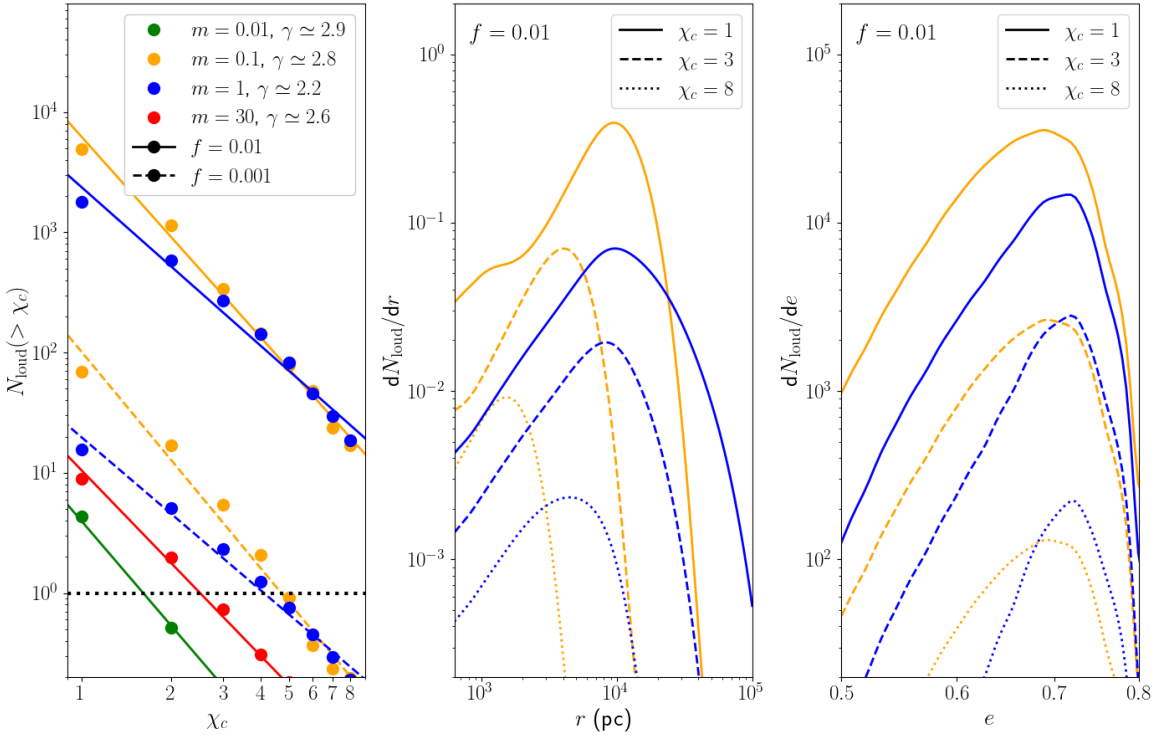


Figure 14: *Left:* the cumulative number $N_{\text{loud}}(> \chi_c)$ of loud Galactic PBH binaries in 5 years of LISA observations as a function of the critical SNR χ_c . The lines represent power law fits to the cumulative counts. The best-fit power law index γ is quoted in the insert. *Middle:* Distribution of the loud PBH binaries as a function of their distance r from the solar system for three values of χ_c . Results are shown for $f = 0.01$ and $m = 0.1, 1$ following the color scheme adopted in the left panel. Notice the correlation between γ and the relative amount of loud sources at large distances (see text) *Right:* Same as the middle panel, but showing the eccentricity distribution of the loud PBH binaries. Note that the area below the distributions is proportional to $N_{\text{loud}}(> \chi_c)$.

As a result, the GW signal is distributed over a relatively small number of harmonics, which makes the source extraction easier. Even though the number of loud sources is small, their mild eccentricity also justifies (a posteriori) the fact that we have ignored the orbital phase in our calculation of the GW signal (i.e. we have not taken into account possible burst-like GW events as discussed in §3.2).

The spatial location of the loud sources could help to discriminate between primordial BH and compact stellar remnants in addition to the (possibly subsolar) mass (and tidal effects, see [117]). Loud PBH sources are the hard binaries located in the “merging” tail of the (log a -log j) plane (see Fig. 13), with time to coalescence mostly concentrated in the range $t_{\text{coal}} \sim 10^2 - 10^5$ yr (with a peak around $10^3 - 10^4$ yr) and semi-major axis $a_0 \lesssim 1$ AU. As a result, disruption is irrelevant for them, and they trace the MW halo (modelled as a NFW profile). The identification of loud PBH binaries is easiest away from the MW bulge and disk, where the contamination by DWDs is lowest.

6 Conclusions

The existence of stellar-mass PBHs is allowed in multi-component dark-matter models provided that they do not exceed a percent of the total dark-matter energy density. In these scenarios, close enough PBH pairs can decouple from the Hubble flow to form PBH binaries, which trace the adiabatic mode. As cosmic structures form, these binaries are accreted onto dark-matter halos and can masquerade as stellar BH binaries. In the MW halo, they contribute to the Galactic GW background, which should be found by future GW experiments.

In this paper, we have computed the GW signal produced by such a hypothetical population of Galactic PBH binaries assuming a monochromatic PBH mass function and a broad range of PBH mass. For this purpose, we have modeled the evolution of PBH binaries from their formation in the early Universe until the present epoch, including the hardening of PBH binaries through GW emission and the disruption of soft binaries by stellar encounters in the MW. Stellar disruption depletes the MW disk and bulge of most of the PBH binaries. In addition to its anisotropy, the present-day population of Galactic PBH binaries is characterized by high values of orbital eccentricity, which distinguishes them from the Galactic DWD population. These large eccentricities increase the amplitude and characteristic frequency of the GW signal produced by Galactic PBH binaries. For a PBH mass in the range $M_{\text{pbh}} \sim 0.1 - 10M_{\odot}$, the GW background produced by Galactic PBH binaries peaks at the millihertz frequencies probed by LISA. Still, the peak of the GW energy density is at least 1-2 orders of magnitude below the effective LISA noise level (obtained upon subtracting resolved Galactic DWDs from the signal) even for PBH a fraction $f = 0.01$. However, proposed experiments like DECIGO and BBO should resolve such a background if it consists of subsolar PBHs with $M_{\text{pbh}} \sim 0.01 - 1M_{\odot}$.

We have estimated the ability of LISA to detect loud Galactic PBH binaries. The SNR cumulative distribution of the loudest sources generally is a power law function of the critical SNR χ_c used to define loud sources. For a PBH fraction $f \lesssim 0.01$ consistent with current limits and a subsolar mass in the range $M_{\text{pbh}} \sim 0.1 - 1M_{\odot}$, the cumulative number of loud sources with $\chi_c = 8$ in 5 years LISA data is ~ 20 . The loud sources are hard PBH binaries tracing the MW particle dark matter profile and, owing to the steepness of the latter, are preferentially located near the center of the MW halo. They are characterized by GW coalescence times of order $10^3 - 10^4$ yr, and eccentricities $e \sim 0.7$ not as high as those of the total population of MW PBH binaries. Therefore, they might masquerade an eccentric, Galactic binary BH population of stellar origin [see, e.g., 115, 116, 118–120]) if their mass is at least a few M_{\odot} . In this case, the spatial location could help discriminate between primordial and stellar binary BHs. Moreover, we have not taken into account PBH binaries forming or involving dynamical capture mechanisms. This later population will resemble stellar populations more and might influence Galactic stellar binary populations as well [e.g. 53].

In the evolution of PBH binaries from their formation until the present epoch, we have taken into account a limited number of physical mechanisms. In particular, we have neglected a possible initial PBH clustering [54–57, 57, 58] and the mass accretion by PBHs [19, 37, 121, 122]. While clustering is not important for small values of f_{pbh} [123], mass accretion onto highly eccentric binaries is not understood well enough to be properly implemented[34]. Furthermore, PBH may be dressed by a cloud of particle particle dark matter of approximately the same mass as the PBH by the time of MR equality, which will affect the distributions [34]. Other relics from the early Universe could also surround them [e.g. 124]. Finally, we

have ignored hardening by 3-body encounters, which may speed up the binary evolution, and even replace one of the PBHs by an astrophysical object. Refs. [34, 46] find that this effect hardly affects the present-day PBH merger rate but, for the whole population of Galactic PBH binaries (which includes many soft binaries), it may be more significant. Further work should also include late-time effects like dynamical capture, and ascertain the extent to which stellar populations and Galactic GW backgrounds of stellar origins are affected by the presence of field PBHs.

Acknowledgments

We are grateful to Gabriele Franciolini, Robert Reischke, Toni Riotto, and Sam Young for helpful discussions. We acknowledge support from the Israel Science Foundation (grant no. 2562/20). Y.B.G. was partly supported by a Leverhulme Trust International Professorship Grant to S. L. Sondhi (No. LIP-2020-014), and partly supported by the Simons Foundation via a Simons Investigator Award to A. A. Schekochihin.

A Gravitational waves from eccentric compact binaries

Eccentricity plays a substantial role in the evolution of a population of PBHs as emphasized here and in previous works [34, 46, 110].

In this Appendix, we discuss the backreaction effect of eccentric GW radiation on the orbital parameter evolution needed in Section 3.2. In addition, we briefly review the vacuum GW emission of an eccentric Keplerian binary used in Section 5.3 to model the GW signal of a Galactic population of PBH binaries. Most of this discussion is based on the seminal works of [67, 68], which is conveniently summarized in [69]. Note that, although we assume a monochromatic PBH mass function throughout this paper, we write below expressions valid for a generic unequal-mass binary with a total mass M and reduced mass μ .

A.1 Orbital evolution

The gravitational wave emission is entirely determined by the mass of the binary components, and the semi-major axis a and eccentricity e of the binary orbit. If the binary hardens through GW emission solely, these orbital parameters evolve via the system of coupled ordinary differential equations (ODEs) in Eq. (3.1) (which involves two distinct timescales t_a and t_e characterizing the evolution of a and e , respectively). The latter can be combined into

$$\frac{da}{de} = \frac{12}{19} a \frac{1 + (73/24)e^2 + (39/96)e^4}{e(1 - e^2)[1 + (121/304)e^2]} . \quad (\text{A.1})$$

This can be integrated analytically to give

$$a(e) = a_* \frac{\mathcal{G}(e)}{\mathcal{G}(e_*)} , \quad (\text{A.2})$$

where the function $\mathcal{G}(e)$ is defined as

$$\mathcal{G}(e) \equiv \frac{e^{12/19}}{1 - e^2} \left(1 + \frac{121}{304}e^2\right)^{870/2299} . \quad (\text{A.3})$$

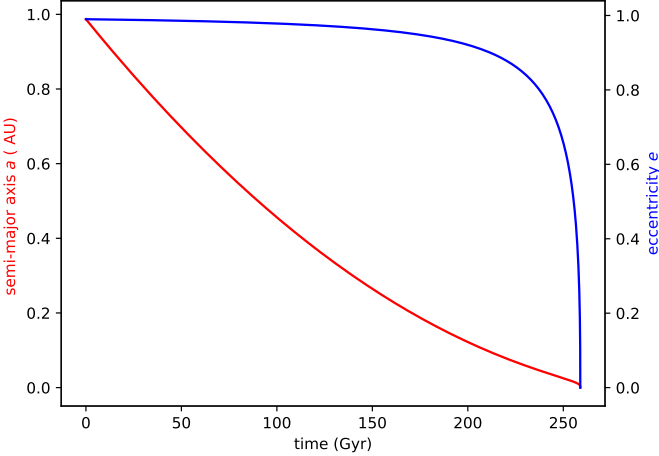


Figure 15: Orbital evolution for a binary with initial semi-major axis $a_i = 1$ AU and eccentricity $e_i = 0.99$ obtained from the solution outlined in §A.2. Note that the decay timescale of the semi-major axis is much shorter than the circularization timescale.

Eq. (A.2) can be used to calculate the time to coalescence t_{coal} of a binary from the relation $\int dt = \int de \frac{dt}{de}$, in which $\frac{de}{dt}$ is given by the second ODE of Eq. (3.1). The dependence of t_{coal} on the initial eccentricity a_* is encoded in the function

$$F(e_*) \equiv \frac{48}{19} \frac{1}{\mathcal{G}^4(e_*)} \int_0^{e_*} de \frac{\mathcal{G}^4(e)(1-e^2)^{5/2}}{e(1+\frac{121}{304}e^2)} \quad (\text{A.4})$$

Finding a numerical solution to the system Eq. (3.1) for a general time $t < t_{\text{coal}}$ is computationally challenging due to the vastly different timescales τ_a and τ_e when e is close to unity. However, it is possible to find a semi-numerical solution for $e(\tau, a_*, e_*)$ as explained below.

A.2 Semi-numerical solution to the eccentric evolution

The solution $e(\tau)$ can be conveniently spelled out in terms of the dimensionless variables $\tilde{a} \equiv a/R_*$ and $\tau \equiv ct/R_*$, where

$$R_*^{-3} \equiv \frac{4G^3\mu M^2}{c^6} \quad (\text{A.5})$$

becomes the Schwarzschild radius $R_* = 2GM/c^2$ for equal mass PBH binaries. The second line of Eq. (3.1) becomes

$$\frac{de}{d\tau} = -\frac{76}{15} \frac{e}{\tilde{a}^4(1-e^2)^{5/2}} \left(1 + \frac{121}{304}e^2\right). \quad (\text{A.6})$$

Substituting $a(e)$ given by Eq. (A.2) into this equation, we can write down an expression for the time τ elapsed since the formation of the PBH binary,

$$\begin{aligned} \tau &= \int_0^\tau d\tau' = \int_{e_i}^e \left(\frac{de'}{d\tau'}\right)^{-1} de' = \frac{15}{76} \int_e^{e_*} de' \frac{\tilde{a}^4(1-e'^2)^{5/2}}{e'[1+(121/304)e'^2]} \\ &= \frac{15}{76} \frac{\tilde{a}_*^4}{\mathcal{G}(e_*)^4} \int_e^{e_*} de' \frac{e'^{29/19}}{(1-e'^2)^{3/2}} \left(1 + \frac{121}{304}e'^2\right)^{1181/2299}. \end{aligned} \quad (\text{A.7})$$

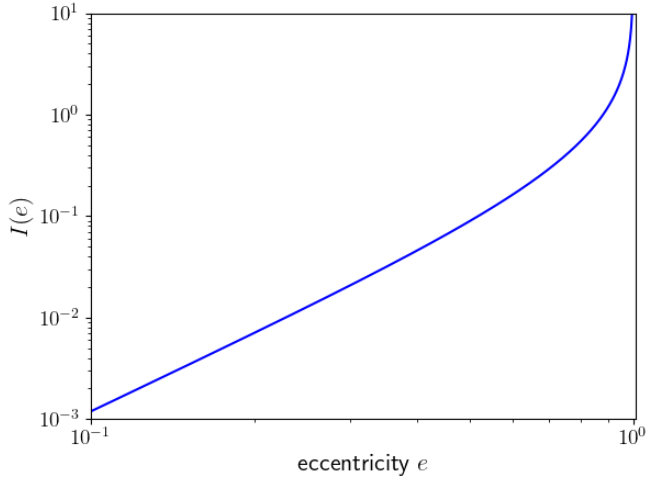


Figure 16: The function $I(e)$ defined in Eq. (A.10). $I(e)$ diverges in the limit $e \rightarrow 1$.

This integral admits a solution in terms of Appell hypergeometric functions of two variables, which read

$$F_1(\alpha, \beta_1, \beta_2, \gamma, x, y) = \sum_{m=0}^{\infty} \sum_{n=0}^{\infty} \frac{(\alpha)_{m+n} (\beta_1)_m (\beta_2)_n}{m! n! (\gamma)_{m+n}} x^m y^n \quad (\text{A.8})$$

where

$$(z)_p = \prod_{k=0}^{p-1} [z - k] \quad (\text{A.9})$$

is the Pochhammer symbol. It is convenient to introduce the function

$$I(e) \equiv \frac{e^{10/19}}{3648} \left(I_0(e) - 3648 A_1(e) - 893 e^2 A_2(e) \right) \quad (\text{A.10})$$

where

$$\begin{aligned} A_1(e) &\equiv F_1 \left(\frac{5}{19}, \frac{1}{2}, \frac{1118}{2299}, \frac{24}{19}, e^2, -\frac{121}{304} e^2 \right) \\ A_2(e) &\equiv F_1 \left(\frac{24}{19}, \frac{1}{2}, \frac{1118}{2299}, \frac{43}{19}, e^2, -\frac{121}{304} e^2 \right) \\ I_0(e) &\equiv \frac{24 \times 2^{2173/2299} \times 19^{1118/2299}}{\sqrt{1-e^2}} \left(304 + 121 e^2 \right)^{1181/2299}. \end{aligned} \quad (\text{A.11})$$

The function $I(e)$ is shown in Fig. 16. The solution to Eq. (A.7) can eventually be recast into the form

$$\tau(e, a_*, e_*) = \frac{15}{76} \frac{\tilde{a}_*^4}{\mathcal{G}(e_*)^4} \left(I(e_*) - I(e) \right). \quad (\text{A.12})$$

The only piece of the calculation left over is the inversion of this expression to find $e(\tau, a_*, e_*)$, which can be carried out using standard numerical routines. The solution for $a(\tau, a_*, e_*)$ then follows from Eq. (A.2), that is, from the knowledge of $e(\tau)$ and the initial conditions (a_*, e_*) . Fig. 15 shows a sample solution for $(a_*, e_*) = (1 \text{ AU}, 0.99)$. For very eccentric orbits, circularization through GW emission is a subdominant effect until the very last stages of the evolution.

A.3 Spectral Distribution

Unlike circular binaries emitting GWs at a frequency $\nu = 2\nu_o$, twice the orbital frequency ν_0 , eccentric binaries emit GWs at all the harmonics $\nu_n = n\nu_0$ of the orbital frequency. In addition, the orbital eccentricity boosts the radiated GW power by a factor of $f(e)$ given by

$$f(e) \equiv \frac{1}{(1-e^2)^{7/2}} \left(1 + \frac{73}{24}e^2 + \frac{37}{96}e^4 \right). \quad (\text{A.13})$$

As a result, the total, orbit-averaged power radiated in GWs becomes

$$P_{e \neq 0} = \frac{32G^4\mu^2M^3}{5c^5a^5} f(e) \equiv P_{e=0} f(e) \quad (\text{A.14})$$

for $e > 0$. For large eccentricities $1 - e \ll 1$, $P_{e \neq 0}$ can be enhanced by orders of magnitude. This power is emitted at the discrete frequencies ν_n and is distributed among them according to

$$P_{e \neq 0} = \sum_{n=1}^{\infty} P_n(e) \quad (\text{A.15})$$

where the n -th harmonic contributes a power $P_n(e)$ given by

$$P_n(e) = P_{e=0} g(n, e). \quad (\text{A.16})$$

The auxiliary functions

$$g(n, e) = \frac{n^4}{32} \left(\left[J_{n-2}(ne) - 2eJ_{n-1}(ne) + \frac{2}{n}J_n(ne) + 2eJ_{n+1}(ne) - J_{n+2}(ne) \right]^2 + (1 - e^2) \left[J_{n-2}(ne) - 2J_n(ne) + J_{n+2}(ne) \right]^2 + \frac{4}{3n^2} \left[J_n(ne) \right]^2 \right), \quad (\text{A.17})$$

where J_n is the Bessel function of the first kind, satisfy the completeness relation

$$\sum_{n=1}^{\infty} g(n, e) = f(e). \quad (\text{A.18})$$

They are helpful for the calculation of the GW energy density produced by a distribution of eccentric binaries (see §5.3).

B Dynamical Friction in the Milky Way Halo

Galactic PBH binaries also harden through Dynamical Friction (DF) with the surrounding PDM distribution. The DF timescale can be estimated with the Chandrasekhar formula [125]¹⁰. Assuming that the PBH binary moves in a circular orbit with velocity $v^2 \simeq GM_{\text{pbh}}/a$ relative to its center-of-mass, the relation $t_{\text{DF}} \sim vM_{\text{pbh}}/F_{\text{DF}}$, where F_{DF} is the magnitude of the DF force, yields

$$t_{\text{DF}}(r) \sim 10^8 \text{ Gyr} \sqrt{m} \left(\frac{a}{\text{AU}} \right)^{-3/2} \left(\frac{\rho_{\text{PDM}}(r)}{10^{-2} \text{ M}_\odot \text{ pc}^{-3}} \right)^{-1} I_{\text{DF}}^{-1}. \quad (\text{B.1})$$

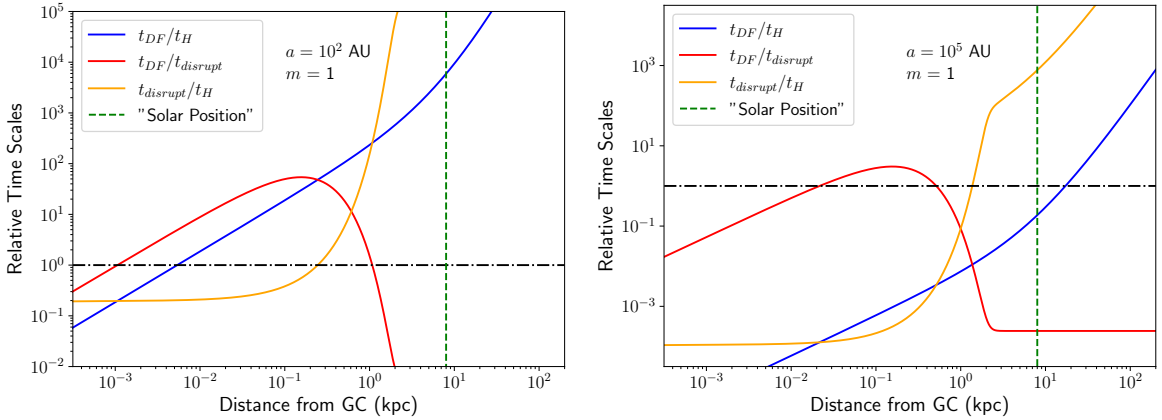


Figure 17: A comparison between the timescales characterizing binary disruption ($t_{disrupt}$) and dynamical friction (t_{DF}) as well as the present-day Hubble time t_H . The various ratios are shown as a function of the separation r from the GC for a soft (*left panel*) and hard (*right panel*) PBH binary with $m = 1$. The vertical (green) dotted line marks the radial distance of our solar system.

Here, r is the distance from the Galactic Center and $\rho_{\text{PDM}}(r)$ is the local PDM density distributed according to the NFW profile Eq. 4.7. Furthermore, I_{DF} is a (velocity-dependent) dimensionless friction coefficient, which we take to be unity.

Fig. 17 compares the PDM-induced DF timescale with the disruption timescale (defined in Section 3.3) and the (present-day) Hubble time for a PBH binary of solar mass ($m = 1$) at different locations in the stellar halo. For relatively hard PBH binaries (left panel), disruption by MW halo stars or single PBHs dominates deep inside the MW virial radius. For $r \gtrsim 1$ kpc, DF is the dominant process but the characteristic timescale t_{DF} is too long to lead to a significant loss of orbital energy within a Hubble time. For softer binaries (right panel), DF is dynamically relevant for separations $1 \lesssim r \lesssim 20$ kpc from the GC. However, given the limited region of the full parameter space this corresponds to, we decided to neglect DF in our evolution model. Note also that, for the comparison with the disruption timescale, we selected a slice through the MW without the stellar disks (i.e. it is approximately orthogonal to the stellar disks). Including the stellar disks increases the effect of disruption and even better justifies the discarding of DF.

References

- [1] S. Hawking, *Gravitationally collapsed objects of very low mass*, *Mon. Not. R. Astron. Soc.* **152** (1971) 75.
- [2] B. J. Carr, *The primordial black hole mass spectrum*, *Astrophys. J.* **201** (1975) 1.
- [3] P. Ivanov, P. Naselsky and I. Novikov, *Inflation and primordial black holes as dark matter*, *Phys. Rev. D* **50** (1994) 7173.
- [4] J. García-Bellido, A. Linde and D. Wands, *Density perturbations and black hole formation in hybrid inflation*, *Phys. Rev. D* **54** (1996) 6040 [[astro-ph/9605094](#)].

¹⁰Although dynamical friction is the gravitational deceleration produced by a nonlocal density wake, local approximations provide a good estimate of the DF force for inhomogeneous systems [see, e.g., 126–128].

- [5] P. Ivanov, *Nonlinear metric perturbations and production of primordial black holes*, *Phys. Rev. D* **57** (1998) 7145 [[astro-ph/9708224](#)].
- [6] LIGO SCIENTIFIC, VIRGO collaboration, B. P. Abbott et al., *Observation of Gravitational Waves from a Binary Black Hole Merger*, *Phys. Rev. Lett.* **116** (2016) 061102 [[1602.03837](#)].
- [7] LIGO SCIENTIFIC, VIRGO collaboration, B. P. Abbott et al., *GWTC-1: A Gravitational-Wave Transient Catalog of Compact Binary Mergers Observed by LIGO and Virgo during the First and Second Observing Runs*, *Phys. Rev. X* **9** (2019) 031040 [[1811.12907](#)].
- [8] LIGO SCIENTIFIC, VIRGO collaboration, R. Abbott et al., *Population Properties of Compact Objects from the Second LIGO-Virgo Gravitational-Wave Transient Catalog*, *Astrophys. J. Lett.* **913** (2021) L7 [[2010.14533](#)].
- [9] S. Bird, I. Cholis, J. B. Muñoz, Y. Ali-Haïmoud, M. Kamionkowski, E. D. Kovetz et al., *Did LIGO detect dark matter?*, *Phys. Rev. Lett.* **116** (2016) 201301 [[1603.00464](#)].
- [10] S. Blinnikov, A. Dolgov, N. K. Porayko and K. Postnov, *Solving puzzles of GW150914 by primordial black holes*, *JCAP* **11** (2016) 036 [[1611.00541](#)].
- [11] M. Sasaki, T. Suyama, T. Tanaka and S. Yokoyama, *Primordial black holes—perspectives in gravitational wave astronomy*, *Class. Quant. Grav.* **35** (2018) 063001 [[1801.05235](#)].
- [12] B. Carr and F. Kuhnel, *Primordial Black Holes as Dark Matter: Recent Developments*, *Ann. Rev. Nucl. Part. Sci.* **70** (2020) 355 [[2006.02838](#)].
- [13] B. Carr, K. Kohri, Y. Sendouda and J. Yokoyama, *Constraints on primordial black holes*, *Rept. Prog. Phys.* **84** (2021) 116902 [[2002.12778](#)].
- [14] P. Villanueva-Domingo, O. Mena and S. Palomares-Ruiz, *A brief review on primordial black holes as dark matter*, *Front. Astron. Space Sci.* **8** (2021) 87 [[2103.12087](#)].
- [15] M. Zumalacarregui and U. Seljak, *Limits on stellar-mass compact objects as dark matter from gravitational lensing of type Ia supernovae*, *Phys. Rev. Lett.* **121** (2018) 141101 [[1712.02240](#)].
- [16] W. DeRocco, E. Frangipane, N. Hamer, S. Profumo and N. Smyth, *Revealing terrestrial-mass primordial black holes with the Nancy Grace Roman Space Telescope*, *Phys. Rev. D* **109** (2024) 023013 [[2311.00751](#)].
- [17] P. Mróz et al., *No massive black holes in the Milky Way halo*, *Nature* **632** (2024) 749 [[2403.02386](#)].
- [18] E. Mediavilla and J. Jiménez-Vicente, *Lensing Constraints on PBHs: Substellar to Intermediate Masses*, [2405.14984](#).
- [19] M. Ricotti, J. P. Ostriker and K. J. Mack, *Effect of Primordial Black Holes on the Cosmic Microwave Background and Cosmological Parameter Estimates*, *Astrophys. J.* **680** (2008) 829 [[0709.0524](#)].
- [20] D. Aloni, K. Blum and R. Flauger, *Cosmic microwave background constraints on primordial black hole dark matter*, *JCAP* **2017** (2017) 017 [[1612.06811](#)].
- [21] B. Bertrand, M. Cuadra-Grzybowski, P. Defraigne, M. Van Camp and S. Clesse, *Observing dark matter clumps and asteroid-mass primordial black holes in the solar system with gravimeters and GNSS networks*, in *Proceedings of the 2023 Gravitation session of the 57th Rencontres de Moriond*, 12, 2023, [2312.14520](#).
- [22] M. Cuadra-Grzybowski, S. Clesse, P. Defraigne, M. Van Camp and B. Bertrand, *Probing primordial black holes and dark matter clumps in the Solar System with gravimeter and Global Navigation Satellite Systems networks*, *Phys. Rev. D* **110** (2024) 063029 [[2403.14397](#)].

[23] M. Andrés-Carcasona, A. J. Iovino, V. Vaskonen, H. Veermäe, M. Martínez, O. Pujolàs et al., *Constraints on primordial black holes from LIGO-Virgo-KAGRA O3 events*, *Phys. Rev. D* **110** (2024) 023040 [[2405.05732](#)].

[24] T. X. Tran, S. R. Geller, B. V. Lehmann and D. I. Kaiser, *Close encounters of the primordial kind: A new observable for primordial black holes as dark matter*, *Phys. Rev. D* **110** (2024) 063533 [[2312.17217](#)].

[25] T. S. Yamamoto, R. Inui, Y. Tada and S. Yokoyama, *Prospects of detection of subsolar mass primordial black hole and white dwarf binary mergers*, *Phys. Rev. D* **109** (2024) 103514 [[2401.00044](#)].

[26] J. Fardeen, P. McGill, S. E. Perkins, W. A. Dawson, N. S. Abrams, J. R. Lu et al., *Astrometric Microlensing by Primordial Black Holes with the Roman Space Telescope*, *Astrophys. J.* **965** (2024) 138 [[2312.13249](#)].

[27] J. B. Dent, B. Dutta and T. Xu, *Multi-messenger Probes of Asteroid Mass Primordial Black Holes: Superradiance Spectroscopy, Hawking Radiation, and Microlensing*, [2404.02956](#).

[28] G. L. Dizon and R. Reyes, *Projected gravitational wave constraints on primordial black hole abundance for extended mass distributions*, [2406.12281](#).

[29] G. Domènech and M. Sasaki, *Probing primordial black hole scenarios with terrestrial gravitational wave detectors*, *Class. Quant. Grav.* **41** (2024) 143001 [[2401.07615](#)].

[30] G. Domènech, *Lectures on Gravitational Wave Signatures of Primordial Black Holes*, in *ICCUB School 2023 on Primordial Black holes*, 7, 2023, [2307.06964](#).

[31] LISA COSMOLOGY WORKING GROUP collaboration, E. Bagui et al., *Primordial black holes and their gravitational-wave signatures*, [2310.19857](#).

[32] T. Nakamura, M. Sasaki, T. Tanaka and K. S. Thorne, *Gravitational waves from coalescing black hole MACHO binaries*, *Astrophys. J. Lett.* **487** (1997) L139 [[astro-ph/9708060](#)].

[33] M. Sasaki, T. Suyama, T. Tanaka and S. Yokoyama, *Primordial Black Hole Scenario for the Gravitational-Wave Event GW150914*, *Phys. Rev. Lett.* **117** (2016) 061101 [[1603.08338](#)].

[34] Y. Ali-Haïmoud, E. D. Kovetz and M. Kamionkowski, *Merger rate of primordial black-hole binaries*, *Phys. Rev. D* **96** (2017) 123523 [[1709.06576](#)].

[35] M. Raidal, V. Vaskonen and H. Veermäe, *Formation of primordial black hole binaries and their merger rates*, [2404.08416](#).

[36] K. J. Mack, J. P. Ostriker and M. Ricotti, *Growth of Structure Seeded by Primordial Black Holes*, *Astrophys. J.* **665** (2007) 1277 [[astro-ph/0608642](#)].

[37] J. R. Rice and B. Zhang, *Cosmological evolution of primordial black holes*, *Journal of High Energy Astrophysics* **13** (2017) 22 [[1702.08069](#)].

[38] D. Inman and Y. Ali-Haïmoud, *Early structure formation in primordial black hole cosmologies*, *Phys. Rev. D* **100** (2019) 083528 [[1907.08129](#)].

[39] E. Vanzan, S. Libanore, L. Valbusa Dall'Armi, N. Bellomo and A. Raccaelli, *Gravitational wave background from primordial black holes in globular clusters*, [2405.13871](#).

[40] D. Maoz and N. Hallakoun, *The binary fraction, separation distribution and merger rate of white dwarfs from SPY*, *Mon. Not. Roy. Astron. Soc.* **467** (2017) 1414 [[1609.02156](#)].

[41] S. H. Strub, L. Ferraioli, C. Schmelzbach, S. C. Stähler and D. Giardini, *Global analysis of LISA data with Galactic binaries and massive black hole binaries*, *Phys. Rev. D* **110** (2024) 024005 [[2403.15318](#)].

[42] S. Phelps, A. Nusser and V. Desjacques, *The Mass of the Milky Way and M31 Using the Method of Least Action*, *Astrophys. J.* **775** (2013) 102 [[1306.4013](#)].

[43] R. J. J. Grand, A. J. Deason, S. D. M. White, C. M. Simpson, F. A. Gómez, F. Marinacci et al., *The effects of dynamical substructure on Milky Way mass estimates from the high velocity tail of the local stellar halo*, *Mon. Not. Roy. Astron. Soc.* **487** (2019) L72 [[1905.09834](#)].

[44] S. Young and C. T. Byrnes, *Initial clustering and the primordial black hole merger rate*, *JCAP* **03** (2020) 004 [[1910.06077](#)].

[45] S. Mukherjee, M. S. P. Meinema and J. Silk, *Prospects of discovering subsolar primordial black holes using the stochastic gravitational wave background from third-generation detectors*, *Mon. Not. Roy. Astron. Soc.* **510** (2022) 6218 [[2107.02181](#)].

[46] M. Raidal, C. Spethmann, V. Vaskonen and H. Veermäe, *Formation and Evolution of Primordial Black Hole Binaries in the Early Universe*, *JCAP* **02** (2019) 018 [[1812.01930](#)].

[47] A. Burrows and D. Vartanyan, *Core-collapse supernova explosion theory*, *Nature (London)* **589** (2021) 29 [[2009.14157](#)].

[48] S. L. Shapiro and S. A. Teukolsky, *Black holes, white dwarfs, and neutron stars: The physics of compact objects*. Wiley & Sons, Hoboken, N.J., 1983, [10.1002/9783527617661](#).

[49] M. Kilic, C. Allende Prieto, W. R. Brown and D. Koester, *The Lowest Mass White Dwarf*, *Astrophys. J.* **660** (2007) 1451 [[astro-ph/0611498](#)].

[50] B. D. Metzger, L. Hui and M. Cantiello, *Fragmentation in Gravitationally Unstable Collapsar Disks and Subsolar Neutron Star Mergers*, *Astrophys. J. Lett.* **971** (2024) L34 [[2407.07955](#)].

[51] LIGO SCIENTIFIC, VIRGO, KAGRA collaboration, R. Abbott et al., *Search for Subsolar-Mass Binaries in the First Half of Advanced LIGO’s and Advanced Virgo’s Third Observing Run*, *Phys. Rev. Lett.* **129** (2022) 061104 [[2109.12197](#)].

[52] M. Prunier, G. Morrás, J. F. N. n. Siles, S. Clesse, J. García-Bellido and E. Ruiz Morales, *Analysis of the subsolar-mass black hole candidate SSM200308 from the second part of the third observing run of Advanced LIGO-Virgo*, *Phys. Dark Univ.* **46** (2024) 101582.

[53] B. Bhalla, B. V. Lehmann, K. Sinha and T. Xu, *Dancing with invisible partners: Three-body exchanges with primordial black holes*, [2408.04697](#).

[54] Y. Ali-Haïmoud, *Correlation Function of High-Threshold Regions and Application to the Initial Small-Scale Clustering of Primordial Black Holes*, *Phys. Rev. Lett.* **121** (2018) 081304 [[1805.05912](#)].

[55] V. Desjacques and A. Riotto, *Spatial clustering of primordial black holes*, *Phys. Rev. D* **98** (2018) 123533 [[1806.10414](#)].

[56] G. Ballesteros, P. D. Serpico and M. Taoso, *On the merger rate of primordial black holes: effects of nearest neighbours distribution and clustering*, *JCAP* **2018** (2018) 043 [[1807.02084](#)].

[57] V. Stasenko, *Redshift evolution of primordial black hole merger rate*, *Phys. Rev. D* **109** (2024) 123546 [[2403.11325](#)].

[58] T. Bringmann, P. F. Depta, V. Domcke and K. Schmidt-Hoberg, *Towards closing the window of primordial black holes as dark matter: The case of large clustering*, *Phys. Rev. D* **99** (2019) 063532 [[1808.05910](#)].

[59] V. De Luca, V. Desjacques, G. Franciolini, A. Malhotra and A. Riotto, *The initial spin probability distribution of primordial black holes*, *JCAP* **2019** (2019) 018 [[1903.01179](#)].

[60] Y. N. Eroshenko, *Gravitational waves from primordial black holes collisions in binary systems*, *J. Phys. Conf. Ser.* **1051** (2018) 012010 [[1604.04932](#)].

[61] K. Hayasaki, K. Takahashi, Y. Sendouda and S. Nagataki, *Rapid merger of binary primordial black holes: An implication for GW150914*, *Publ. Astron. Soc. Jap.* **68** (2016) 66 [[0909.1738](#)].

[62] O. Özsoy and G. Tasinato, *Inflation and Primordial Black Holes*, *Universe* **9** (2023) 203 [[2301.03600](#)].

[63] M. Kawasaki and V. Takhistov, *Primordial Black Holes and the String Swampland*, *Phys. Rev. D* **98** (2018) 123514 [[1810.02547](#)].

[64] J. Garcia-Bellido, A. D. Linde and D. Wands, *Density perturbations and black hole formation in hybrid inflation*, *Phys. Rev. D* **54** (1996) 6040 [[astro-ph/9605094](#)].

[65] C. Germani and I. Musco, *Abundance of Primordial Black Holes Depends on the Shape of the Inflationary Power Spectrum*, *Phys. Rev. Lett.* **122** (2019) 141302 [[1805.04087](#)].

[66] B. J. Carr, K. Kohri, Y. Sendouda and J. Yokoyama, *New cosmological constraints on primordial black holes*, *Phys. Rev. D* **81** (2010) 104019 [[0912.5297](#)].

[67] P. C. Peters and J. Mathews, *Gravitational radiation from point masses in a Keplerian orbit*, *Phys. Rev.* **131** (1963) 435.

[68] P. C. Peters, *Gravitational Radiation and the Motion of Two Point Masses*, Ph.D. thesis, Caltech, 1964.

[69] M. Maggiore, *Gravitational Waves. Vol. 1: Theory and Experiments*. Oxford University Press, 2007, [10.1093/acprof:oso/9780198570745.001.0001](#).

[70] J. Goodman and P. Hut, *Binary - single star scattering. 5. Steady state binary distribution in a homogeneous static background of single stars*, *Astrophys. J.* **403** (1993) 271.

[71] Y. B. Ginat and H. B. Perets, *Analytical, Statistical Approximate Solution of Dissipative and Nondissipative Binary-Single Stellar Encounters*, *Phys. Rev. X* **11** (2021) 031020.

[72] B. Carr, S. Clesse, J. Garcia-Bellido, M. Hawkins and F. Kuhnel, *Observational evidence for primordial black holes: A positivist perspective*, *Phys. Rept.* **1054** (2024) 1 [[2306.03903](#)].

[73] D. C. Heggie and P. Hut, *Binary - single star scattering. 4. Analytic approximations and fitting formulae for cross-sections and reaction rates*, *Astrophys. J. Suppl.* **85** (1993) 347.

[74] Y. B. Ginat and H. B. Perets, *Binaries are softer than they seem: effects of an external potential on the scattering dynamics of binaries*, *Mon. Not. R. Astron. Soc.* **508** (2021) 190 [[2108.01085](#)].

[75] J. Heisler and S. Tremaine, *The influence of the Galactic tidal field on the Oort comet cloud*, *Icarus* **65** (1986) 13.

[76] E. Grishin and H. B. Perets, *Chaotic dynamics of wide triples induced by galactic tides: a novel channel for producing compact binaries, mergers, and collisions*, *Mon. Not. R. Astron. Soc.* **512** (2022) 4993 [[2112.11475](#)].

[77] S. Modak and C. Hamilton, *Eccentricity dynamics of wide binaries - I. The effect of Galactic tides*, *Mon. Not. R. Astron. Soc.* **524** (2023) 3102 [[2303.15531](#)].

[78] C. Flynn, J. Holmberg, L. Portinari, B. Fuchs and H. Jahreiss, *On the mass-to-light ratio of the local Galactic disc and the optical luminosity of the Galaxy*, *Mon. Not. Roy. Astron. Soc.* **372** (2006) 1149 [[astro-ph/0608193](#)].

[79] J. Bovy and H.-W. Rix, *A Direct Dynamical Measurement of the Milky Way's Disk Surface Density Profile, Disk Scale Length, and Dark Matter Profile at 4 kpc $\lesssim R \lesssim$ 9 kpc*, *Astrophys. J.* **779** (2013) 115 [[1309.0809](#)].

[80] T. C. Llicquia and J. A. Newman, *Improved Estimates of the Milky Way's Stellar Mass and Star Formation Rate from Hierarchical Bayesian Meta-Analysis*, *Astrophys. J.* **806** (2015) 96 [[1407.1078](#)].

[81] M. Cautun, A. Benítez-Llambay, A. J. Deason, C. S. Frenk, A. Fattahi, F. A. Gómez et al., *The milky way total mass profile as inferred from Gaia DR2*, *Mon. Not. R. Astron. Soc.* **494** (2020) 4291 [[1911.04557](#)].

[82] J. Binney and S. Tremaine, *Galactic Dynamics: Second Edition*. Princeton University Press, Princeton, N.J., 2008.

[83] S. Young and A. S. Hamers, *The impact on distant fly-bys on the rate of binary primordial black hole mergers*, *JCAP* **10** (2020) 036 [[2006.15023](#)].

[84] V. Korol, N. Hallakoun, S. Toonen and N. Karnesis, *Observationally driven Galactic double white dwarf population for LISA*, *Mon. Not. Roy. Astron. Soc.* **511** (2022) 5936 [[2109.10972](#)].

[85] A. P. Cooper et al., *Galactic stellar haloes in the CDM model*, *Mon. Not. Roy. Astron. Soc.* **406** (2010) 744 [[0910.3211](#)].

[86] H.-N. Lin and X. Li, *The Dark Matter Profiles in the Milky Way*, *Mon. Not. Roy. Astron. Soc.* **487** (2019) 5679 [[1906.08419](#)].

[87] E. Valenti, M. Zoccali, O. A. Gonzalez, D. Minniti, J. Alonso-García, E. Marchetti et al., *Stellar density profile and mass of the Milky Way bulge from VVV data*, *Astron. Astrophys.* **587** (2016) L6 [[1510.07425](#)].

[88] C. Allende Prieto, *The Stellar Population of the Thin Disk*, *IAU Symp.* **265** (2010) 304 [[0911.3598](#)].

[89] M. Bennett and J. Bovy, *Vertical waves in the solar neighbourhood in Gaia DR2*, *Mon. Not. R. Astron. Soc.* **482** (2019) 1417 [[1809.03507](#)].

[90] GRAVITY Collaboration, R. Abuter, A. Amorim, M. Bauböck, F. Baganoff, J. P. Berger et al., *Constraining particle acceleration in Sgr A* with simultaneous GRAVITY, Spitzer, NuSTAR, and Chandra observations*, *Astron. Astrophys.* **654** (2021) A22 [[2107.01096](#)].

[91] Y. B. Ginat, V. Desjacques, R. Reischke and H. B. Perets, *Probability distribution of astrophysical gravitational-wave background fluctuations*, *Phys. Rev. D* **102** (2020) 083501 [[1910.04587](#)].

[92] Y. B. Ginat, R. Reischke, I. Rapoport and V. Desjacques, *Frequency-domain distribution of astrophysical gravitational-wave backgrounds*, *Phys. Rev. D* **109** (2024) 083526 [[2305.09372](#)].

[93] S. Staelens and G. Nelemans, *Likelihood of white dwarf binaries to dominate the astrophysical gravitational wave background in the mHz band*, *Astron. Astrophys.* **683** (2024) A139 [[2310.19448](#)].

[94] E. S. Phinney, *A Practical Theorem on Gravitational Wave Backgrounds*, *arXiv e-prints* (2001) astro [[astro-ph/0108028](#)].

[95] T. Robson, N. J. Cornish and C. Liu, *The construction and use of LISA sensitivity curves*, *Class. Quant. Grav.* **36** (2019) 105011 [[1803.01944](#)].

[96] N. J. Cornish, *Detecting a stochastic gravitational wave background with the Laser Interferometer Space Antenna*, *Phys. Rev. D* **65** (2002) 022004 [[gr-qc/0106058](#)].

[97] S. Babak, A. Petiteau and M. Hewitson, *LISA Sensitivity and SNR Calculations*, [2108.01167](#).

[98] M. Georgousi, N. Karnesis, V. Korol, M. Pieroni and N. Stergioulas, *Gravitational waves from double white dwarfs as probes of the milky way*, *Mon. Not. Roy. Astron. Soc.* **519** (2022) 2552 [[2204.07349](#)].

[99] S. Lin, B. Hu, X.-H. Zhang and Y.-X. Liu, *White dwarf binary modulation can help stochastic gravitational wave background search*, *Sci. China Phys. Mech. Astron.* **66** (2023) 299512 [[2212.14519](#)].

[100] G. Boileau, A. Lamberts, N. J. Cornish and R. Meyer, *Spectral separation of the stochastic gravitational-wave background for LISA in the context of a modulated Galactic foreground*, *Mon. Not. Roy. Astron. Soc.* **508** (2021) 803 [[2105.04283](#)].

[101] S. Nissanke, M. Vallisneri, G. Nelemans and T. A. Prince, *Gravitational-wave emission from compact Galactic binaries*, *Astrophys. J.* **758** (2012) 131 [[1201.4613](#)].

[102] T. Wagg, F. S. Broekgaarden, S. E. de Mink, L. A. C. van Son, N. Frankel and S. Justham, *Gravitational Wave Sources in Our Galactic Backyard: Predictions for BHBH, BHNS, and NSNS Binaries Detectable with LISA*, *Astrophys. J.* **937** (2022) 118 [[2111.13704](#)].

[103] A. J. Farmer and E. S. Phinney, *The gravitational wave background from cosmological compact binaries*, *Mon. Not. Roy. Astron. Soc.* **346** (2003) 1197 [[astro-ph/0304393](#)].

[104] J. Wu and J. Li, *Subtraction of the confusion foreground and parameter uncertainty of resolvable galactic binaries on the networks of space-based gravitational-wave detectors*, *Phys. Rev. D* **108** (2023) 124047 [[2307.05568](#)].

[105] E. A. Huerta et al., *Complete waveform model for compact binaries on eccentric orbits*, *Phys. Rev. D* **95** (2017) 024038 [[1609.05933](#)].

[106] A. M. Knee, I. M. Romero-Shaw, P. D. Lasky, J. McIver and E. Thrane, *A Rosetta Stone for Eccentric Gravitational Waveform Models*, *Astrophys. J.* **936** (2022) 172 [[2207.14346](#)].

[107] L. Barack and C. Cutler, *LISA capture sources: Approximate waveforms, signal-to-noise ratios, and parameter estimation accuracy*, *Phys. Rev. D* **69** (2004) 082005 [[gr-qc/0310125](#)].

[108] M. Enoki and M. Nagashima, *The Effect of Orbital Eccentricity on Gravitational Wave Background Radiation from Cosmological Binaries*, *Prog. Theor. Phys.* **117** (2007) 241 [[astro-ph/0609377](#)].

[109] E. A. Huerta, S. T. McWilliams, J. R. Gair and S. R. Taylor, *Detection of eccentric supermassive black hole binaries with pulsar timing arrays: Signal-to-noise ratio calculations*, *Phys. Rev. D* **92** (2015) 063010 [[1504.00928](#)].

[110] S. Bondani, M. Bonetti, L. Broggi, F. Haardt, A. Sesana and M. Dotti, *Gravitational waves from an eccentric population of primordial black holes orbiting Sgr A**, *Phys. Rev. D* **109** (2024) 043005 [[2303.12868](#)].

[111] L. Wen, *On the eccentricity distribution of coalescing black hole binaries driven by the Kozai mechanism in globular clusters*, *Astrophys. J.* **598** (2003) 419 [[astro-ph/0211492](#)].

[112] S. Kawamura et al., *Current status of space gravitational wave antenna DECIGO and B-DECIGO*, *PTEP* **2021** (2021) 05A105 [[2006.13545](#)].

[113] G. M. Harry, P. Fritschel, D. A. Shaddock, W. Folkner and E. S. Phinney, *Laser interferometry for the big bang observer*, *Class. Quant. Grav.* **23** (2006) 4887.

[114] K. Yagi and N. Seto, *Detector configuration of DECIGO/BBO and identification of cosmological neutron-star binaries*, *Phys. Rev. D* **83** (2011) 044011 [[1101.3940](#)].

[115] Z. Xuan, S. Naoz, B. Kocsis and E. Michaely, *Stochastic gravitational wave background from highly-eccentric stellar-mass binaries in the millihertz band*, *Phys. Rev. D* **110** (2024) 023020 [[2403.04832](#)].

[116] Z. Xuan, S. Naoz, B. Kocsis and E. Michaely, *Detecting Gravitational Wave Bursts from Stellar-mass Binaries in the mHz Band*, *Astrophys. J.* **965** (2024) 148 [[2310.00042](#)].

[117] F. Crescimbeni, G. Franciolini, P. Pani and A. Riotto, *Can we identify primordial black holes? Tidal tests for subsolar-mass gravitational-wave observations*, *Phys. Rev. D* **109** (2024) 124063 [[2402.18656](#)].

[118] D. J. D’Orazio and J. Samsing, *Black Hole Mergers From Globular Clusters Observable by LISA II: Resolved Eccentric Sources and the Gravitational Wave Background*, *Mon. Not. Roy. Astron. Soc.* **481** (2018) 4775 [[1805.06194](#)].

[119] X. Fang, T. A. Thompson and C. M. Hirata, *The Population of Eccentric Binary Black Holes: Implications for mHz Gravitational-wave Experiments*, *Astrophys. J.* **875** (2019) 75 [[1901.05092](#)].

[120] N. Gupte et al., *Evidence for eccentricity in the population of binary black holes observed by LIGO-Virgo-KAGRA*, [2404.14286](#).

[121] M. Ricotti, *Bondi Accretion in the Early Universe*, *Astrophys. J.* **662** (2007) 53 [[0706.0864](#)].

[122] V. De Luca, G. Franciolini, P. Pani and A. Riotto, *Constraints on primordial black holes: The importance of accretion*, *Phys. Rev. D* **102** (2020) 043505 [[2003.12589](#)].

[123] V. De Luca, V. Desjacques, G. Franciolini and A. Riotto, *The clustering evolution of primordial black holes*, *JCAP* **2020** (2020) 028 [[2009.04731](#)].

[124] H. Nishikawa, E. D. Kovetz, M. Kamionkowski and J. Silk, *Primordial-black-hole mergers in dark-matter spikes*, *Phys. Rev. D* **99** (2019) 043533 [[1708.08449](#)].

[125] S. Chandrasekhar, *Dynamical Friction. I. General Considerations: the Coefficient of Dynamical Friction.*, *Astrophys. J.* **97** (1943) 255.

[126] S. Tremaine and M. D. Weinberg, *Dynamical friction in spherical systems.*, *Mon. Not. R. Astron. Soc.* **209** (1984) 729.

[127] M. D. Weinberg, *Self-gravitating response of a spherical galaxy to sinking satellites*, *Mon. Not. R. Astron. Soc.* **239** (1989) 549.

[128] G. Eytan, V. Desjacques and R. Buehler, *Acoustic wake in an isothermal profile: dynamical friction and gravitational wave emission*, *arXiv e-prints* (2024) arXiv:2405.18117 [[2405.18117](#)].